NASA CR-54620, 1967
PWA-2749

EXPERIMENTAL EVALUATION OF TRANSONIC STATORS

PRELIMINARY ANALYSIS AND DESIGN REPORT

PREPARED FOR

NATIONAL AERONAUTICS AND
SPACE ADMINISTRATION

CONTRACT NAS3-7614

Pratt & Whitney Aircraft DIVISION OF UNITED AIRCRAFT CORPORATION
EAST HARTFORD CONNECTICUT

Requests for copies of this report should be referred to

National Aeronautics and Space Administration
Office of Scientific and Technical Information
Attention: USS-A
Washington, D. C. 20546

NASA CR-54620, 1967
PWA-2749

EXPERIMENTAL EVALUATION OF TRANSONIC STATORS PRELIMINARY ANALYSIS AND DESIGN REPORT

by

N. T. Monsarrat
M. J. Keenan

prepared for

NATIONAL AERONAUTICS AND SPACE ADMINISTRATION

CONTRACT NAS3-7614

Technical Management
NASA Lewis Research Center
Cleveland, Ohio
Lewis Project Manager: William L. Beede
Lewis Research Advisor: Calvin L. Ball

Pratt & Whitney Aircraft DIVISION OF UNITED AIRCRAFT CORPORATION

EAST HARTFORD, CONNECTICUT

#51

FOREWORD

This report was produced in accordance with NASA contract NAS3-7614 for NASA Lewis Research Center, Cleveland, Ohio. It describes the aerodynamic and mechanical design and related analyses for a flow-generating rotor and three sets of research stators.

ABSTRACT

A flow-generating rotor has been designed under NASA contract NAS3-7614 to enable three transonic stators to be tested. The stators were designed by NASA in conjunction with the Contractor. Design analyses were conducted and the results indicate that the rotor will produce the required inlet flow to the stators. Structural and vibration analyses indicate that resonances and critical speeds occur outside the operating range and that the component stresses will be well within the capabilities of the materials used. Design details of the flow generation rotor and the three transonic stators are presented.

TABLE OF CONTENTS

LIST OF ILLUSTRATIONS

LIST OF ILLUSTRATIONS (Cont'd)

LIST OF TABLES

I. SUMMARY

A flow-generating rotor has been designed under NASA contract NAS3-7614 to enable three transonic stators to be tested. The stators were designed by NASA in conjunction with the Contractor.

The aerodynamic design of the rotor was based on the stator flow requirements, specific contract requirements, and existing facility requirements. The resulting rotor was designed for a pressure ratio of 1.55, maximum relative velocity vector turning of 16 degrees past axial at the hub and a constant outer diameter of 31 inches. The design tip speed is 1197 ft/sec and the design inlet flow per unit annulus area is 36.0 lb/ft^2, corresponding to a rotor root inlet diameter of 16.6 inches. The rotor inlet swirl required to produce the proper flow necessitates the use of inlet guide vanes, which have also been designed.

The airfoil designs for the inlet guide vane and rotor were determined. The inlet guide vane was designed for an aspect ratio of 1.5 and a chord of 3.5 inches, which was held constant from root to tip. There are 27 vanes designed as NACA M 400 series airfoils since the inlet Mach number is only about 0.46. The degree of turning is large, but analysis indicates that the exact value achieved is not critical.

The rotor was designed for an aspect ratio of 2.14 and a chord of 4.2 inches, which was held constant from root to tip. Twenty-eight blades with double-circular-arc sections will be used.

The three sets of stators were designed for an inlet relative Mach number of 1.1 at the hub and an inlet flow angle of 48°. The blading was designed to turn the flow to the axial direction at all radii. A hub solidity of 1.91 was selected along with an aspect ratio of 2.06 which resulted in 63 blades having a chord of 2.155 inches. One of the three sets of stators employs double circular-arc blade sections. The other two employ a blade shape in which the forward section of the blade and the rearward section are circular arc sections with different radii, designated as multiple circular arc blades. These two stator blade rows were designed for two chordwise distributions of loading.

Mechanical design included a structural and vibration analysis. The only serious resonance in the running range is 4E, that is, the vibratory response corresponding to four excitations per revolution. There is nothing in the flow path, however, which will excite the blades in a high 4E stress. The 5E and 6E resonances, also in the running range are not so serious as the lower orders, nor are these excitations found in the flow path. Centrifugal stress, gas bending stress, and stress produced by untwist are all well below the capabilities of the AMS 4928 titanium alloy to be used for the blades. The fatigue characteristics of the alloy are more than adequate for the anticipated vibration. All critical speeds are outside the operating range.

II. INTRODUCTION

Future aircraft turbojet powerplants will require lightweight, highly loaded axial-flow compressors which provide high efficiency over a wide range of operating conditions. To achieve these goals, new concepts must be employed. One such concept is the operation of compressor blading at high Mach numbers. Rotors have been operated transonically quite successfully, with some production engines now having relative Mach numbers as high as 1.3 at the blade tips. Transonic stators, however, have not been so successful, and stator Mach numbers in production engines have been limited to 0.8.

The test results from a research stator blade row designed for high subsonic inlet Mach numbers were reported in Reference 1. Losses of approximately double that measured in stator blade rows operated at low subsonic inlet flow and of equivalent loadings were indicated. These high losses were attributed to shock waves occurring within the blade row as a result of the high subsonic inlet flow. The blade shape employed in this research stator blade row was of the double circular arc type.

In view of these difficulties, work is being conducted under NASA contract NAS3-7614 to evaluate a new airfoil designed by NASA and expected to be suitable for operation at high Mach numbers. Three stators will be studied in this investigation. One of these stators will have a double circular arc blade section such as used for the stator of Reference 1. The other two employ a blade shape in which the forward and rearward sections are circular arcs with different radii. The concept of these multiple circular arc blade shapes is to minimize the turning in the forward portion of the blade and thereby decrease the magnitude of shock losses. A guide vane and a flow generation rotor to produce the desired stator inlet flow were designed by the Contractor. This report presents the design of the flow-generation system and of the three research stator blade rows.

The nomenclature used in this report conforms to that of the NASA SP-36 Aerodynamic Design of Axial Flow Compressors and is presented in Appendix A of this report.

III. AERODYNAMIC DESIGN

Because the designs of the flow-generating device and the research stators are closely related, iterations were required to match these components properly. In general, the flow-generating device was designed to be compatible with the stator specifications, and to require as little modification to existing facilities as possible. Slight compromises were made in the stator design requirements specified in the contract in arriving at a satisfactory final design. The stator final design values are given below.

Tip Diameter (Inches)	31
Inlet Hub-to-Tip Ratio	0.7
Inlet Flow Angle at Hub (Degrees)	47.7
Inlet Absolute Mach Number at Hub	1.097
Exit Flow Angle at All Radii (Degrees)	0
Axial Velocity Ratio at Hub	0.89
Aspect Ratio	2.06

Specific contract requirements applicable to the rotor design were that the rotor produce a constant total pressure ratio from hub to tip and that the design be based on existing technology.

The rotor pressure ratio was set at 1.55, constant from root to tip, which is well within the capabilities of existing technology and is ample to ensure that the test stand duct losses will not limit rig operation.

Consideration of the stator inlet requirements in conjunction with the selected pressure ratio determined the absolute velocity vector at the rotor root exit, and, hence, the relative velocity vector was variable only as a function of the wheel speed. It was determined that, to meet the existing technology requirement, the relative velocity vector should not be extended much beyond 15 degrees past axial. The resulting design has a rotor root exit wheel speed of 643 ft/sec and a velocity vector 16 degrees past axial.

With exit swirl and wheel speed established for rotor root sections, Euler's equations were used to calculate the rotor inlet swirl required to meet the pressure ratio requirement. A free vortex rotor inlet swirl was selected to define the radial variation of turning for the inlet guide vane.

A constant outer diameter was selected for the rig to reduce cost, to reduce rotor tip clearance problems, and to provide a smooth platform from which to mount interstage probing instrumentation. An outer diameter of 31 inches was selected. This size was large enough to permit application of results to future gas turbine engine designs without concern for scale effects and was compatible with size limitations of the test facility selected for this investigation.

Combining the established rotor exit hub wheel speed of 643 ft/sec with the specified stator inlet hub-to-tip ratio of 0.7 and a constant outer diameter permitted the rotor tip speed to be calculated. The value obtained was 1197 ft/sec.

The only remaining portion of the flowpath to be established was the inlet annulus area. Increasing the inlet flow per unit annulus area reduces the camber of the inlet guide vanes and the rotor blades, as well as the flowpath curvature. The maximum acceptable value is limited by the state of the art. Hence, a value of 36.0 lb/ft^2 was selected for the inlet flow per unit annulus area. This flow is well within the state of the art and provides acceptable camber and flowpath curvature values. The corresponding rotor root inlet diameter is 16.6 inches.

The inlet and exit sections of the rig were designed primarily to be compatible with existing test stand hardware. A standard bell-mouth from a low pressure compressor rig was selected and requires only a slight converging fairing to join it to the rig inlet. The exit section will be faired to the existing test stand collector.

The final flowpath is shown in Figure 1. Detailed calculations for the flowpath were made with a computer program used to provide the basic aerodynamic design of Pratt & Whitney Aircraft axial flow compressors. This program provides three-dimensional axisymmetric compressible flow solutions of the continuity, energy, and radial equilibrium equations. Curvature, enthalpy, and entropy gradient terms are included in the equilibrium calculation, and provisions are made for adding angular momentum terms behind a stationary blade row. The detailed computer results are presented in Appendix B; the calculation stations are shown in Figure B-1. Note that the aerodynamic design values are presented for two different stator configurations. One set of values is for a stator blade row employing the double-circular-arc (DCA) blade shape and the other set for the stators which will employ the new blade shape designated multiple-circular-arc (MCA). The differences noted in the aerodynamic design are a result of different levels of estimated loss for the two types of blade shape and estimated losses from these shapes will be discussed in detail in a later section.

The aspect ratio for the inlet guide vane is 1.5 and, for the rotor, 2.14. A 1.75 inch axial spacing, which is 50 percent of the assumed inlet guide vane chord, was left between the inlet guide vane and the rotor. This spacing is larger than that which might be used in an actual engine, but it provides ample room for instrumentation. A space of 1.5 inches was left between the rotor and the test stator, also to provide space for instrumentation.

Figure 1 shows support struts in both the inlet and exit sections. Passage blockage terms have been included in the design calculation. No adverse aerodynamic effects resulted because of strut locations and/or size.

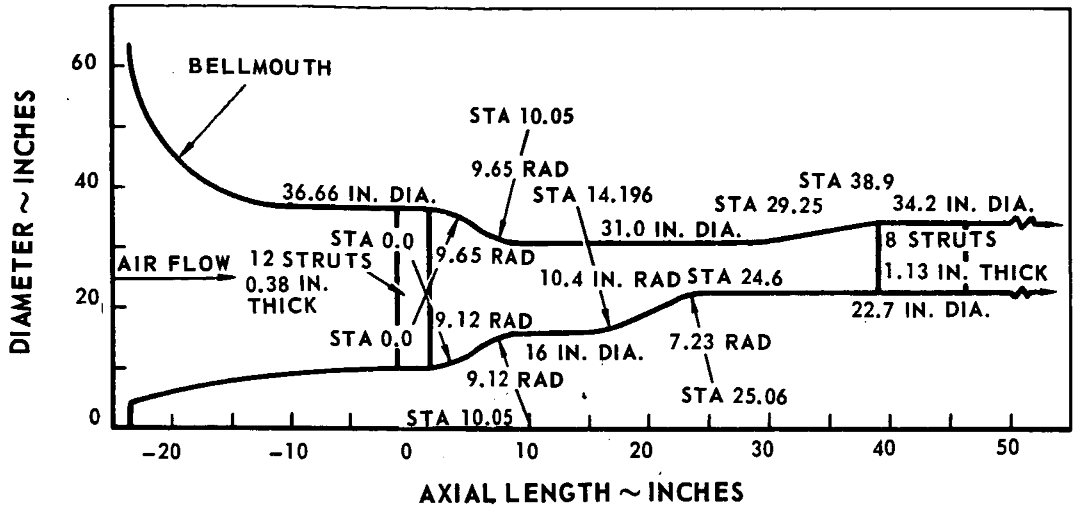

Figure 1 Test Rig Flowpath

Losses for the inlet guide vane were estimated on the basis of the existing engine and rig inlet guide vane data shown in Figure 2. As shown, the estimated guide vane losses are roughly averages of the existing data except at the root and tip. No attempt was made to simulate the end wall boundary layers except for introduction of a displacement thickness.

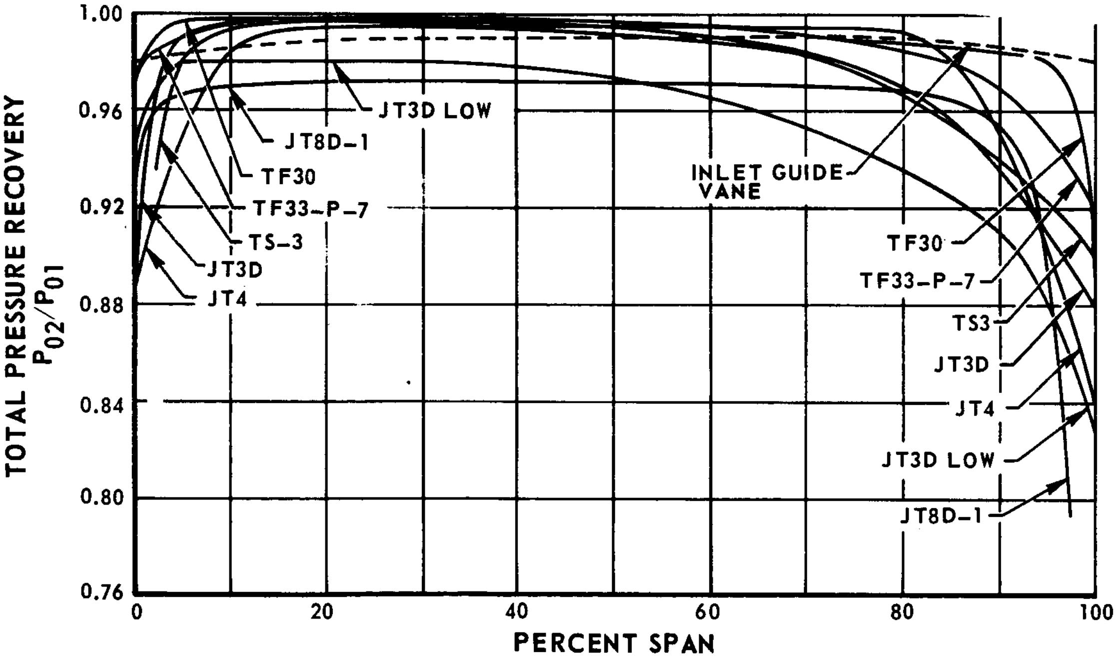

Figure 2 Inlet Guide Vane Pressure Recovery for Various Pratt & Whitney Aircraft Engines and Rigs Shown with Estimated Recovery for Subject Inlet Guide Vane.

The design rotor efficiency distribution along the span was determined on the basis of test data from several single-stage rigs (Figure 3). Also shown are the significant parameters for each of the rotors. It can be seen that the efficiency estimated for this flow-generating rotor is comparable to that measured for other rotors of similar design.

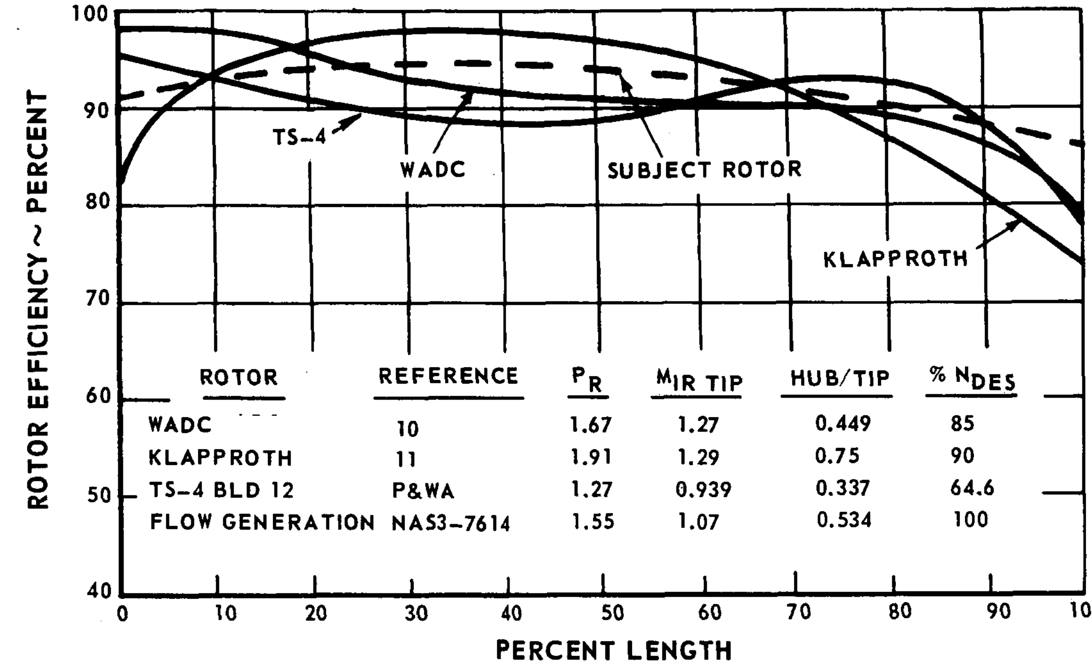

ROTOR	REFERENCE	P_R	M_{IR} TIP	HUB/TIP	% N_{DES}
WADC	10	1.67	1.27	0.449	85
KLAPPROTH	11	1.91	1.29	0.75	90
TS-4 BLD 12	P&WA	1.27	0.939	0.337	64.6
FLOW GENERATION	NAS3-7614	1.55	1.07	0.534	100

Figure 3 Rotor Efficiency of Various Single - Stage Rigs and Design Efficiency of Subject Rotor.

A study was made to determine the effect of the efficiency of the rotor on the flow conditions into the stator. Speed, flow rate, and rotor turning were held constant. The results of the study are shown in Figure 4. Four different assumed rotor efficiency profiles are shown in Figure 4a with design rotor efficiency profile labeled profile number 1. The effects of the four rotor efficiency profiles on stator inlet flow angle, Mach number and stator loading are shown in Figures 4b, 4c and 4d respectively. For a uniform decrease of 2 points in rotor efficiency as shown by profile number 2 (4a), the stator hub inlet air angle decreases by 0.6° (4b), the stator inlet Mach number increases by 0.017 at the hub (4c), and the stator aerodynamic loading ($\Delta P/q$) at this radial location decreases by 0.021 (4d). The tip values of stator inlet flow angle, Mach number, and loading change from the design values by -1.0°, +0.008, and -0.007 respectively. For a uniform drop in rotor efficiency of 4 percentage points, as shown by profile 3, the hub values of stator inlet flow angle (4b), Mach number (4c), and loading (4d) change -1.5°, +0.033 and -0.043 respectively, relative to the design values. At the tip the changes were -2.0°, +0.014 and -0.017 respectively. Profile 4 represents the design efficiency in the hub region, dropping to a 4 point loss in tip efficiency. This profile represents performance if rotor tip loss were underestimated. For this profile the hub values of stator inlet flow angle, Mach number, and loading change by -0.6°, +0.022, and -0.022 respectively from the design values, and the tip values change +0.1°, +0.003, and +0.003 respectively.

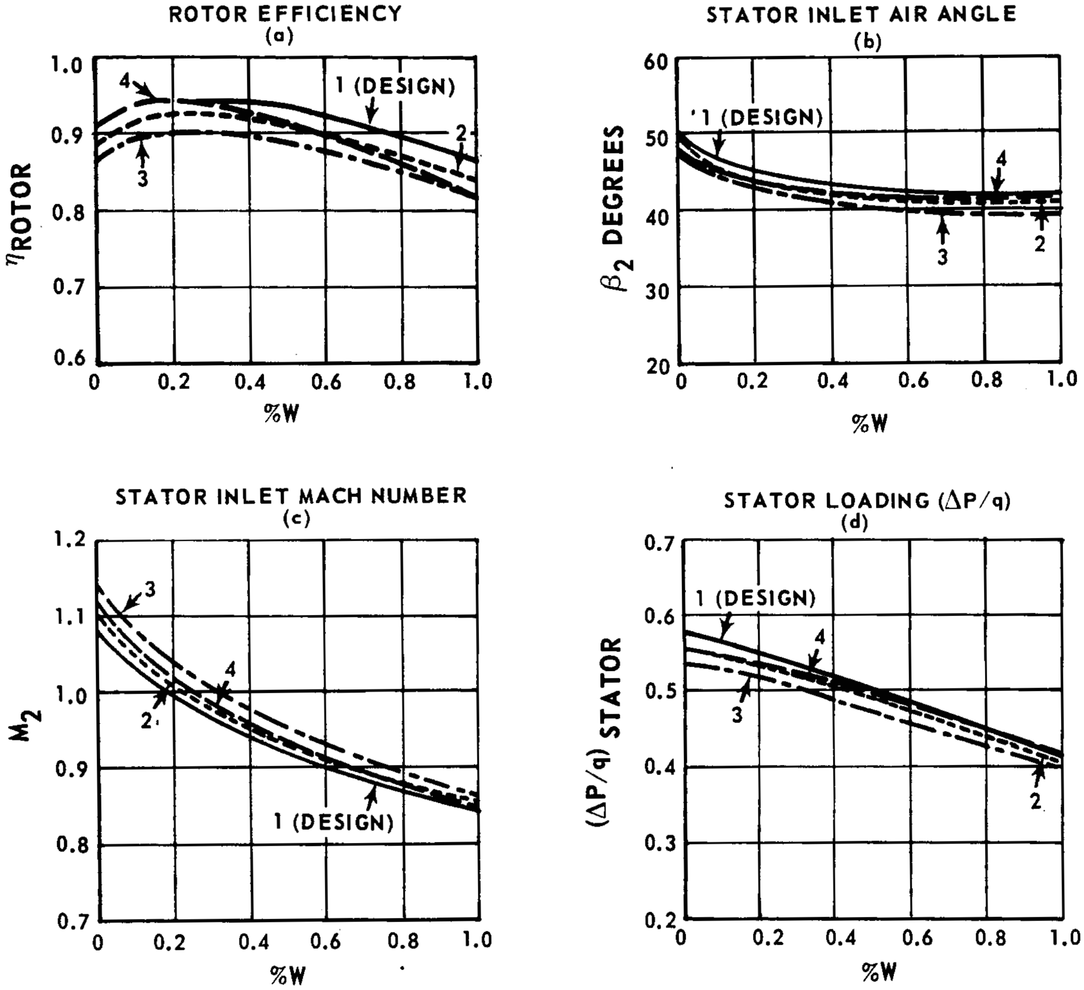

Figure 4 Effect of Rotor Efficiency Profile on Stator Inlet Conditions

It is apparent from the analysis results that the rotor efficiency profile does not significantly affect the stator inlet conditions.

It is noted that the effect of reduced rotor efficiency on stator operating conditions is generally similar to the effect of reduced back pressure on the stage; consequently, the changes in $\Delta P/q$ and air angle would be minimized by operating the stage at lower than design flow.

IV. AIRFOIL DESIGN

A. Inlet Guide Vane

The inlet guide vane aspect ratio was chosen to provide an adequate chord to ensure sufficient structural strength. The resulting chord is 3.5 inches and is constant from root to tip. The number of vanes was set at 27 to produce acceptable aerodynamic loading and to prevent the inlet guide vane from exciting resonant vibrations in the rotor or test stator at test conditions. The loading of the inlet guide vane as indicated by the Zwiefel coefficient is shown in Figure 5. A Zwiefel coefficient of 0.9 is considered to be an acceptable maximum value, and the coefficient of the subject vane is considerably below this value. The light loading should result in relatively small wakes behind the vane.

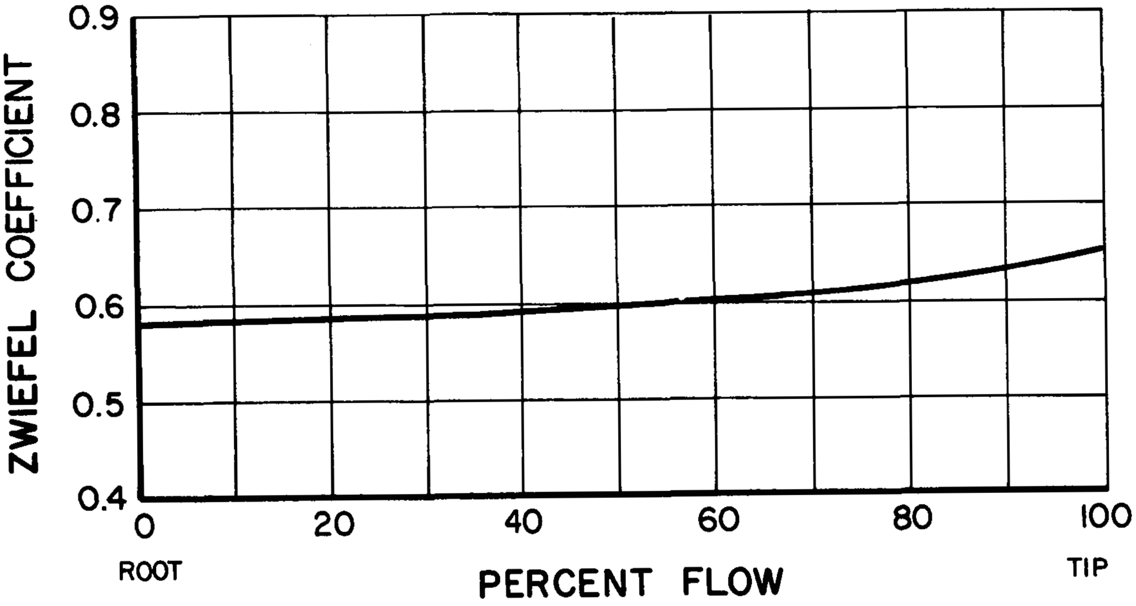

Figure 5 Inlet Guide Vane Loading Parameter

The airfoil thickness-to-chord ratio was made constant from root to tip at 0.09. This ratio will result in acceptably low losses since the inlet Mach number is only about 0.46. NACA M 400 series airfoils were selected, primarily on the basis of inlet Mach number.

This inlet guide vane is not typical of Pratt & Whitney Aircraft designs and was not designed using the normal Pratt & Whitney Aircraft inlet guide vane design system. To design this vane, the data from all inlet guide vane cascade tests conducted at Pratt & Whitney Aircraft were reviewed. Some of these data are shown in Figure 6. The vane was designed on the basis of the applicable data, and the result was then compared with that arrived at by utilizing the Pratt & Whitney Aircraft inlet guide vane design system. Extrapolating the designs arrived at by the Pratt & Whitney Aircraft design system to the turnings required by the subject inlet guide vane resulted in designs which essentially agreed with the subject design.

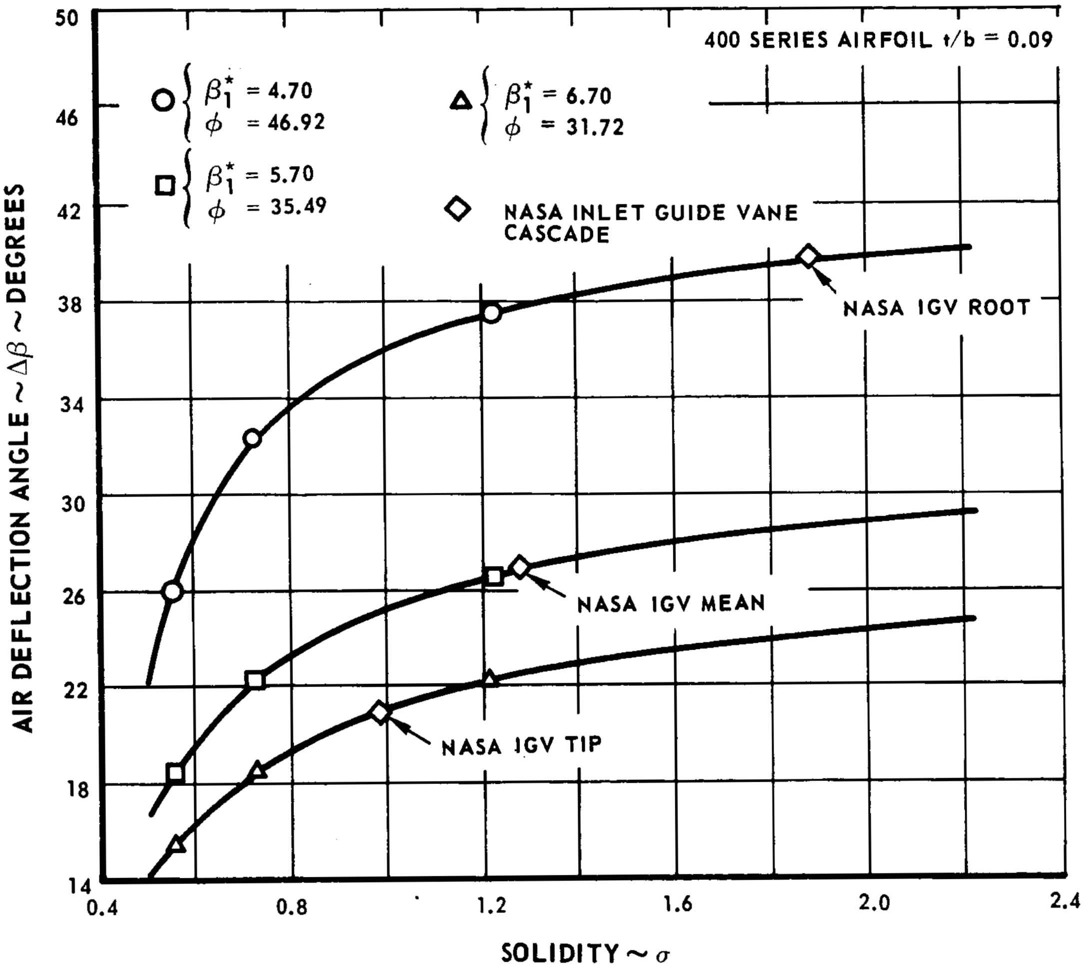

Figure 6 Test Summary Used for Design of Inlet Guide Vane

The inlet guide vane has an unusually large root turning requirement as compared to other inlet guide vanes designed by Pratt & Whitney Aircraft (Figure 7). Because it may be difficult to produce the exact degree of turning required, a study was made to determine the effect of varying guide vane deviation on the test stator.

For this study, the speed, flow, and rotor relative exit angle were held constant and the inlet guide vane turning varied. The results of this study are shown in Figure 8. As shown, for 4 degrees underturning, the stator root Mach number changed by 0.034, and the inlet air angle changes by 0.7 degrees. The maximum changes occur at the tip where the Mach number changes by 0.04 and the inlet air angle changes by 3 degrees. The effects of small errors in turning, therefore, are considered acceptable.

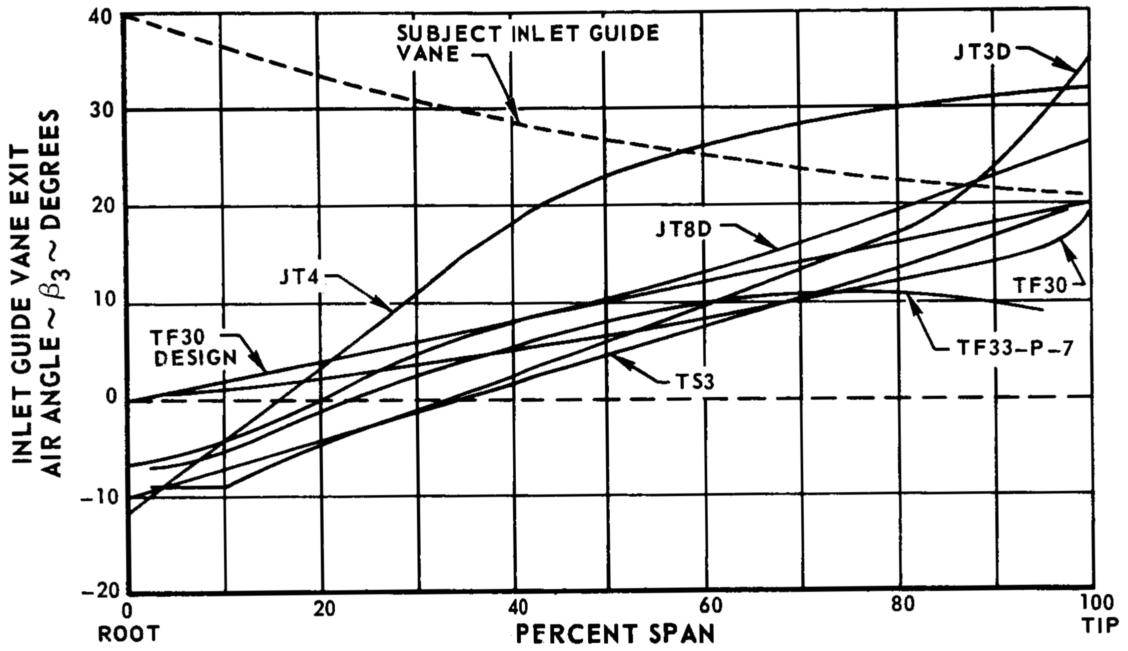

Figure 7 Pratt & Whitney Aircraft Rig and Engine Inlet Guide Vane Exit Air Angles

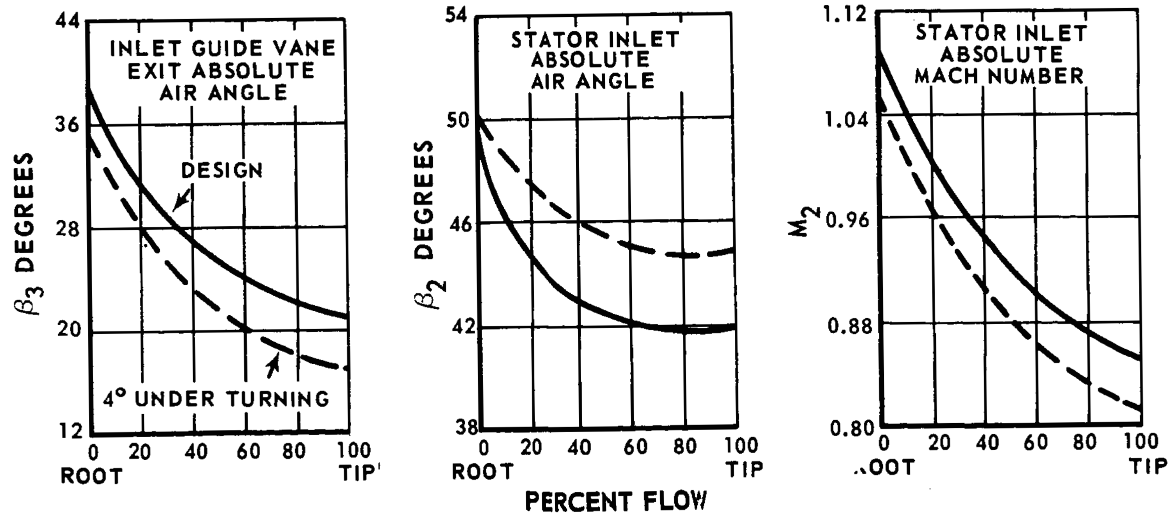

Figure 8 Effect of Inlet Guide Vane Turning Angle on Stator Inlet Conditions

Secondary flow effects were calculated for the inlet guide vane using the method of Lieblein and Ackley[2]. This work, including boundary layer calculations, is discussed in detail in Appendix C. As a consequence of the calculations, three degrees of camber were added at both the root and tip. The change in camber is shown in Figure 9.

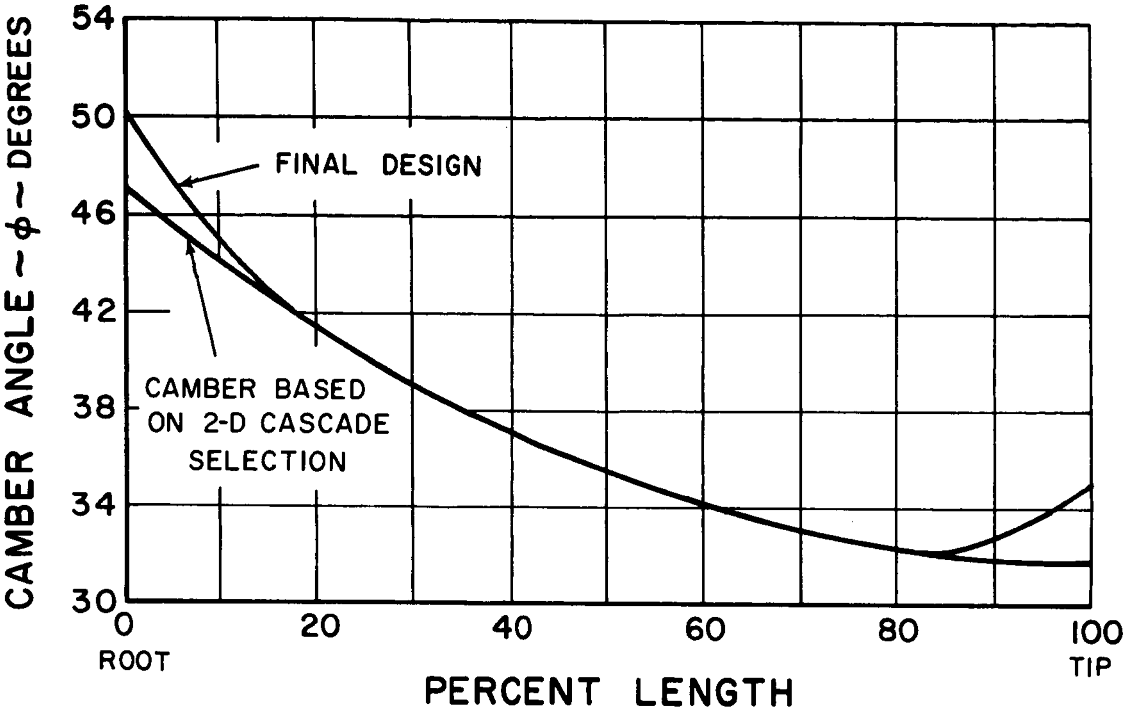

Figure 9 Inlet Guide Vane Camber

The incidence and deviation angles for the inlet guide vane are shown in Figure 10. The inlet guide vane geometry is tabulated in Appendix D.

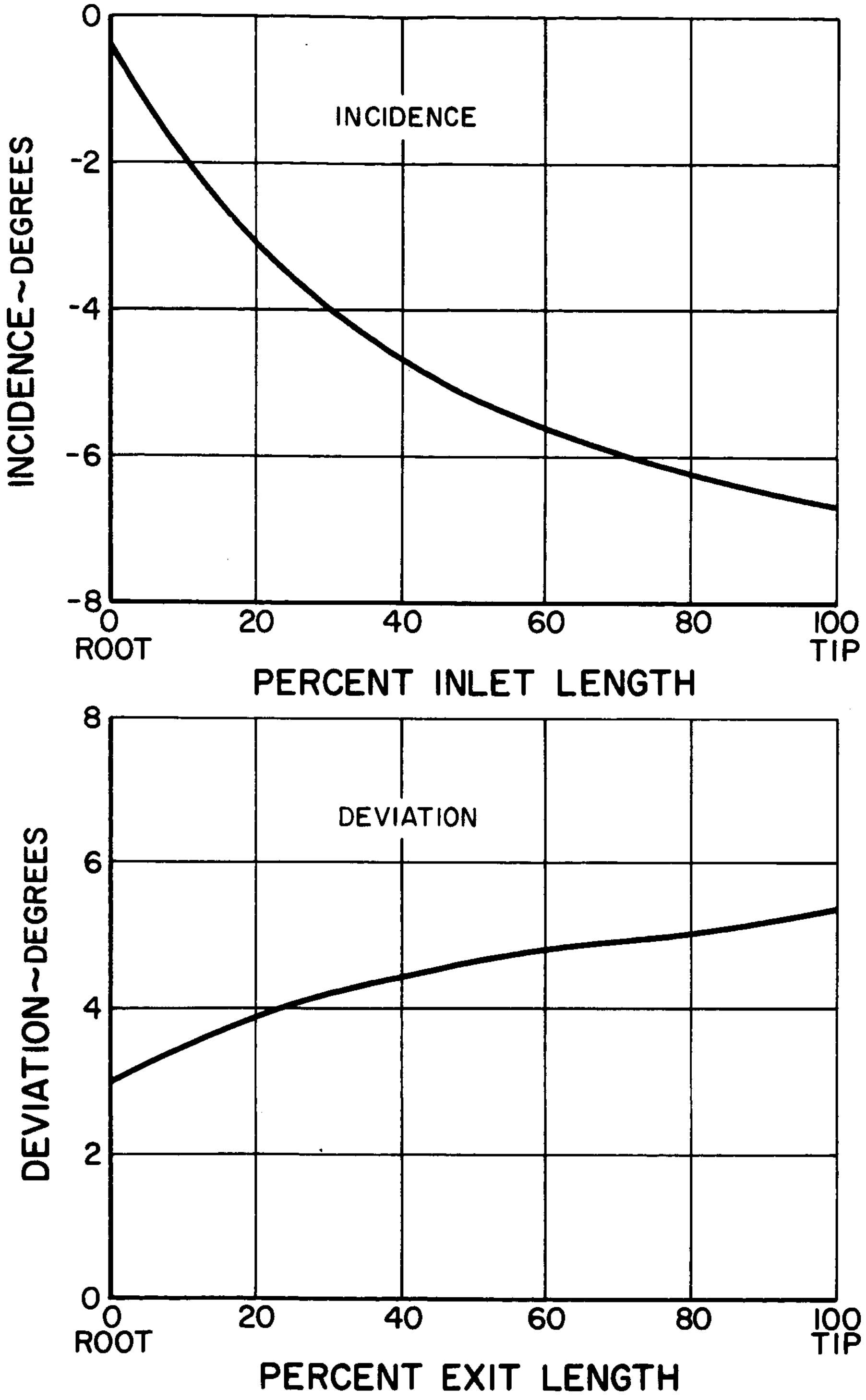

Figure 10 Inlet Guide Vane Incidence and Deviation Angles

B. Rotor

The rotor aerodynamic conditions were translated to the slant planes of the rotor leading and trailing edges. This was accomplished by performing aerodynamic calculations for three axial locations at both the inlet and exit of the rotor. These locations bracketed the rotor blade edges. The results were then interpolated between the axial locations to obtain conditions along the slant plane. The interpolation results are shown in Figures 11, 12, and 13.

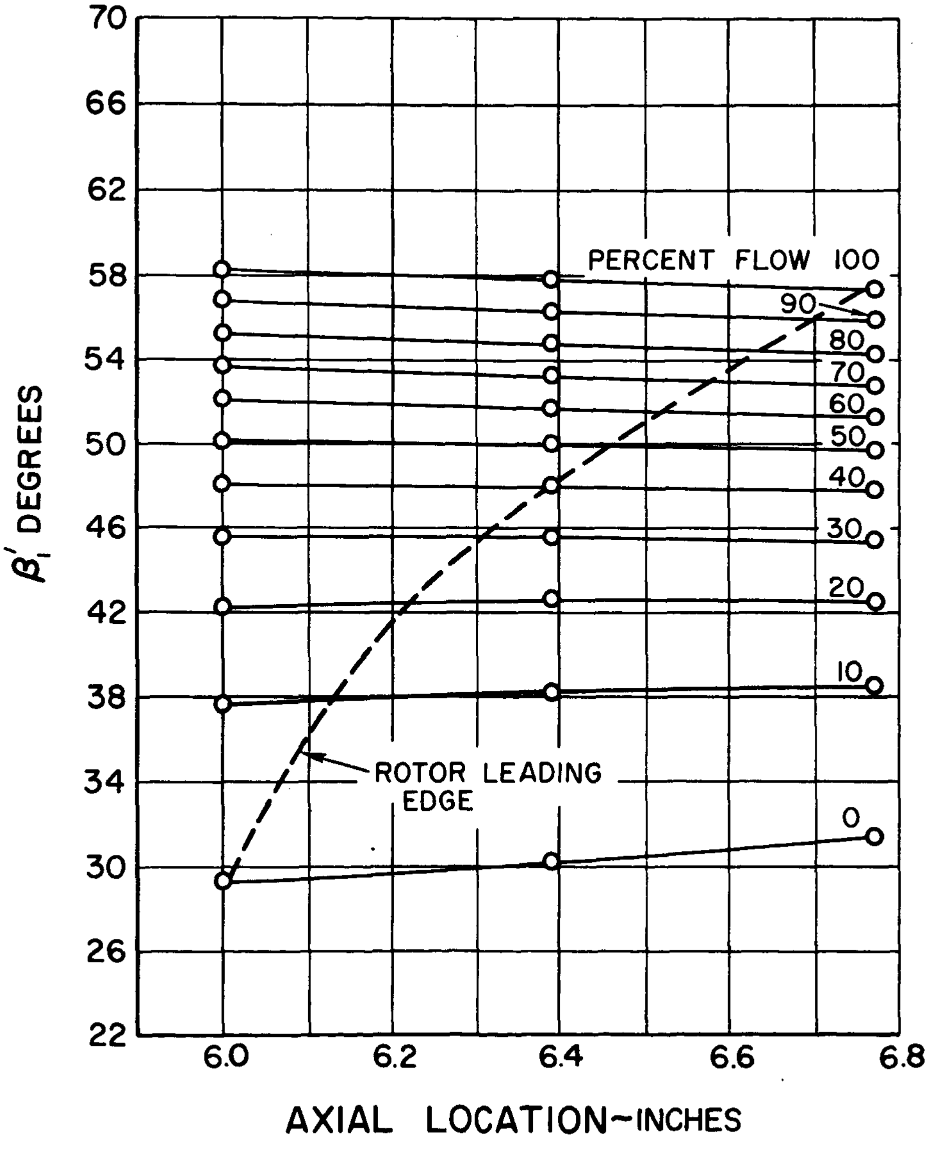

Figure 11 β_1' at Rotor Leading Edge

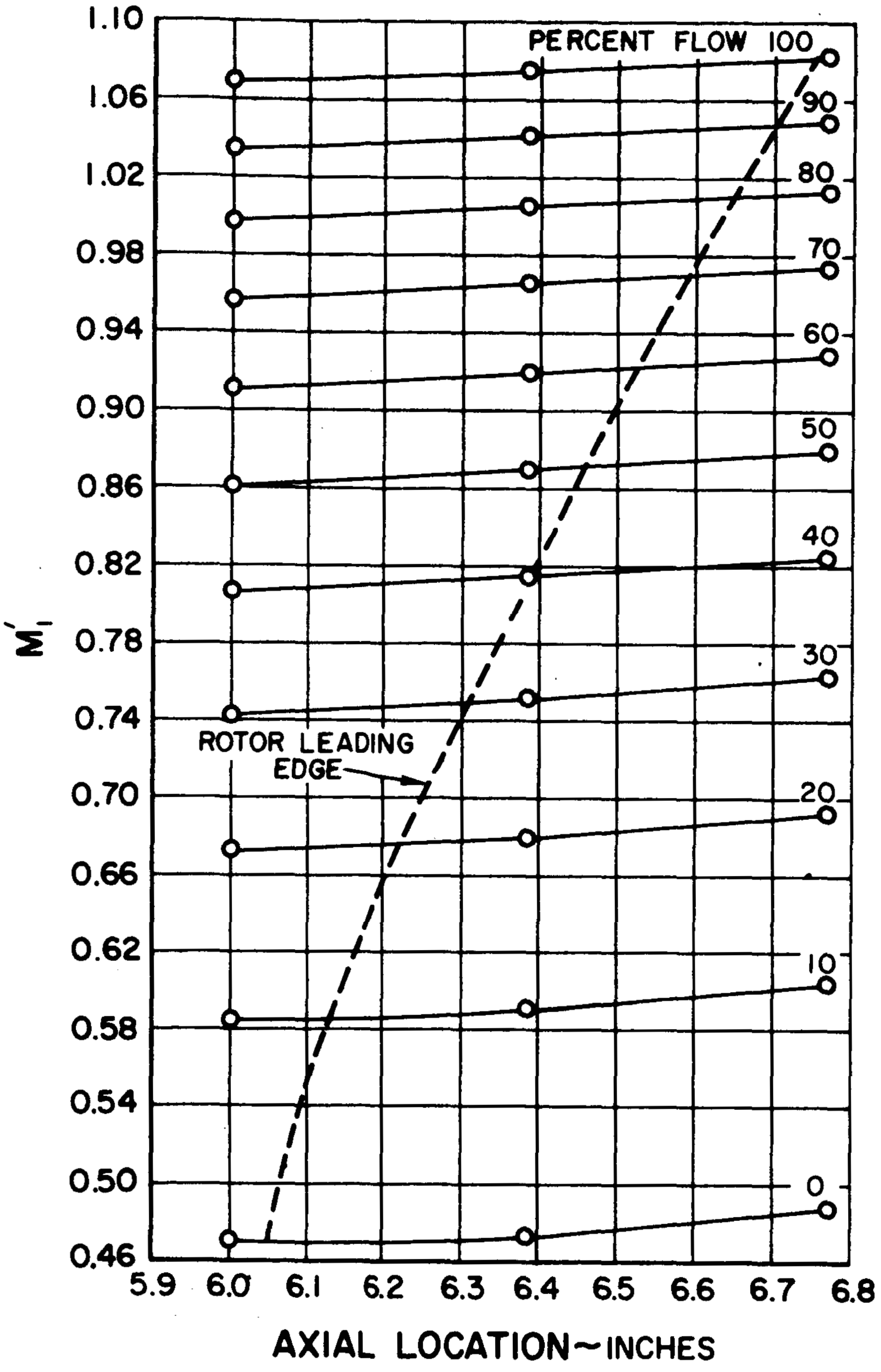

Figure 12 Inlet M_1' at Rotor Leading Edge

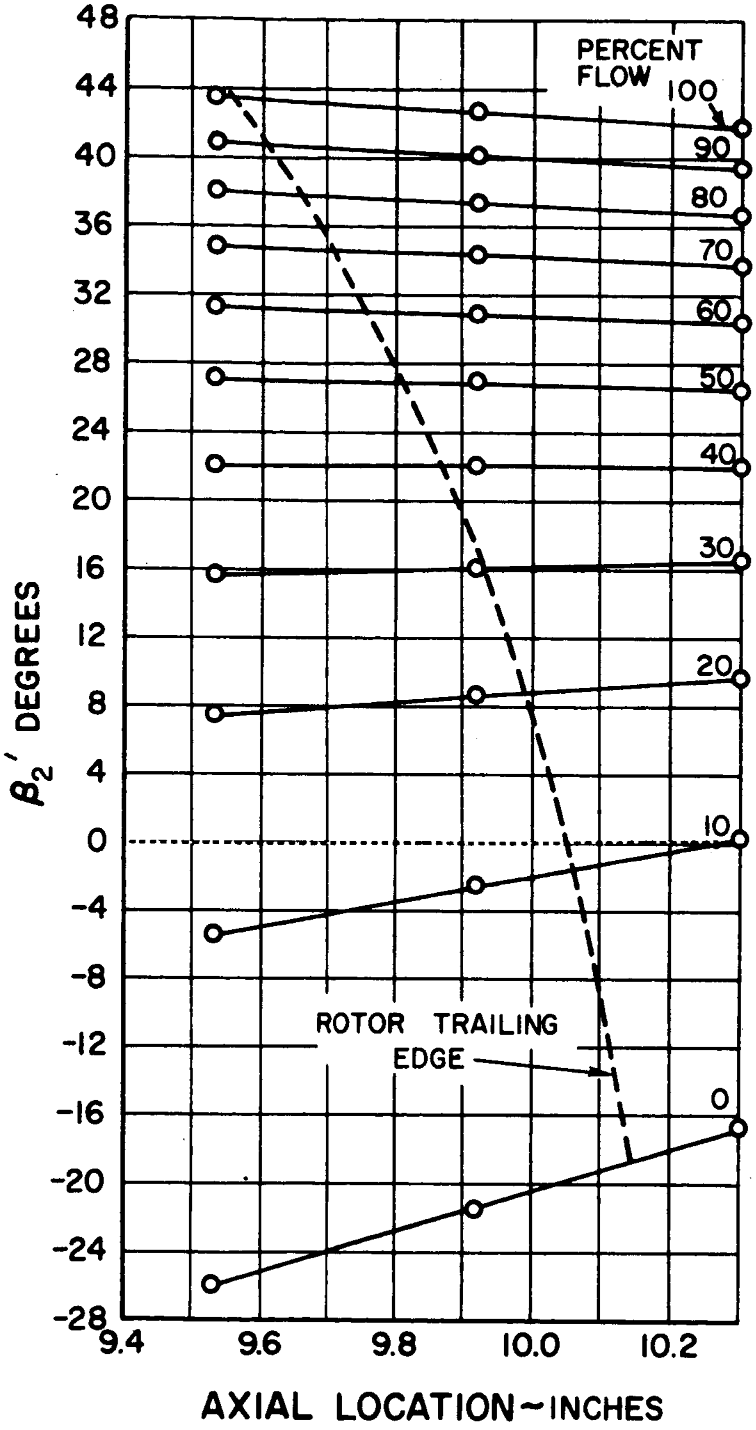

Figure 13 β_2' at Rotor Trailing Edge

Aerodynamic, structural, and flutter conditions led to the selection of an aspect ratio of 1.5. This resulted in a 4.2-inch rotor chord held constant from hub to tip.

The number of rotor blades was established on the basis of the rotor diffusion factor. The variations in solidity and diffusion factor at the hub and tip are shown in Figure 14. Twenty-eight blades were selected, resulting in a tip diffusion factor of 0.43.

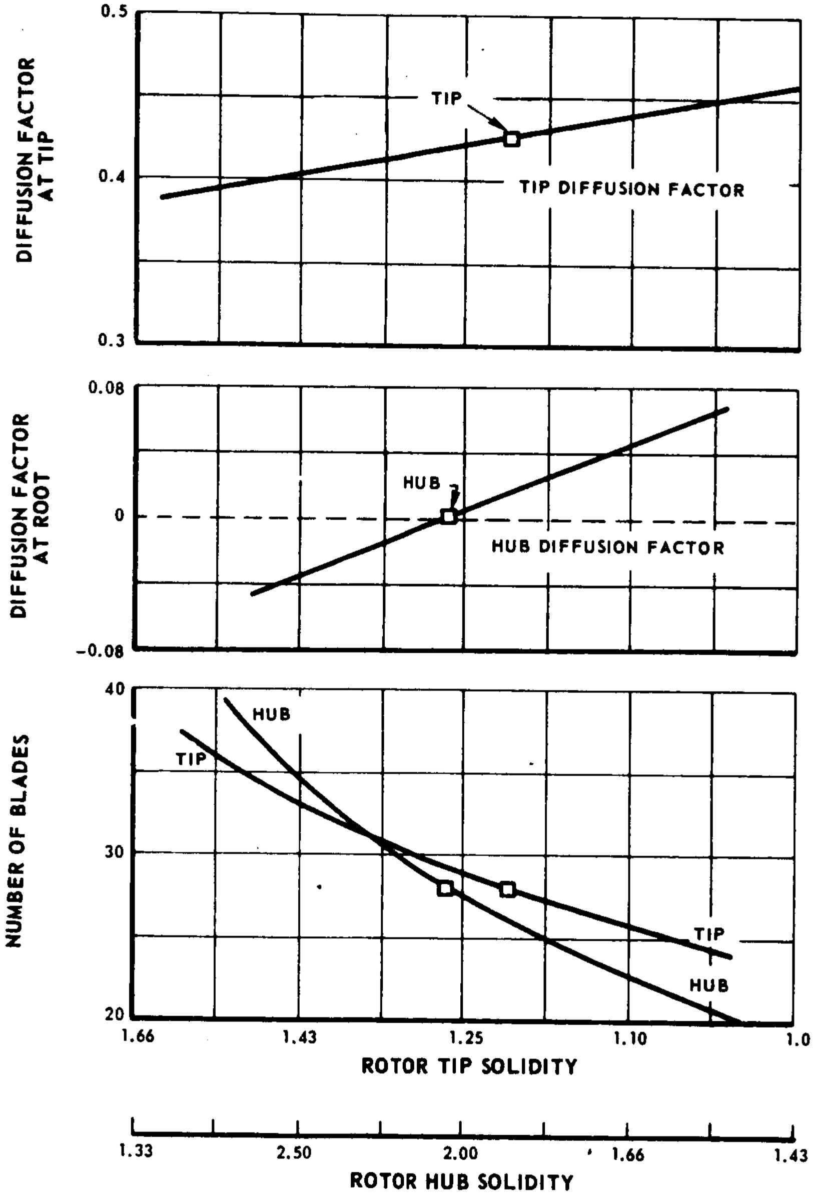

Figure 14 Variation in Solidity and Diffusion Factor at Blade Hub and Tip as a Function of the Number of Rotor Blades

The airfoil series was selected from Mach number considerations. For a rotor tip relative Mach number of 1.07, a double circular arc section will provide a low loss level.

The rotor thickness-to-chord ratio varies linearly from 0.08 at the root to 0.04 at the tip. This design is conservative structurally, but does not degrade the aerodynamic performance of the rotor.

The rotor sections were obtained by the following method:

1. Values for β_1', M_1', and β_2' were obtained from Figures 11, 12, and 13 for a particular streamline. Values of solidity were then established for a streamline at the average of the rotor inlet and exit diameters.
2. The incidence and deviation angles which would provide the minimum losses were selected using the NASA 3-D system presented in NASA SP-36[3] and the previously established conditions. The incidence angle was later modified to reflect the results of high speed cascade testing. The final values are shown in Figure 15, together with the minimum loss angles indicated by the NASA 3-D system.

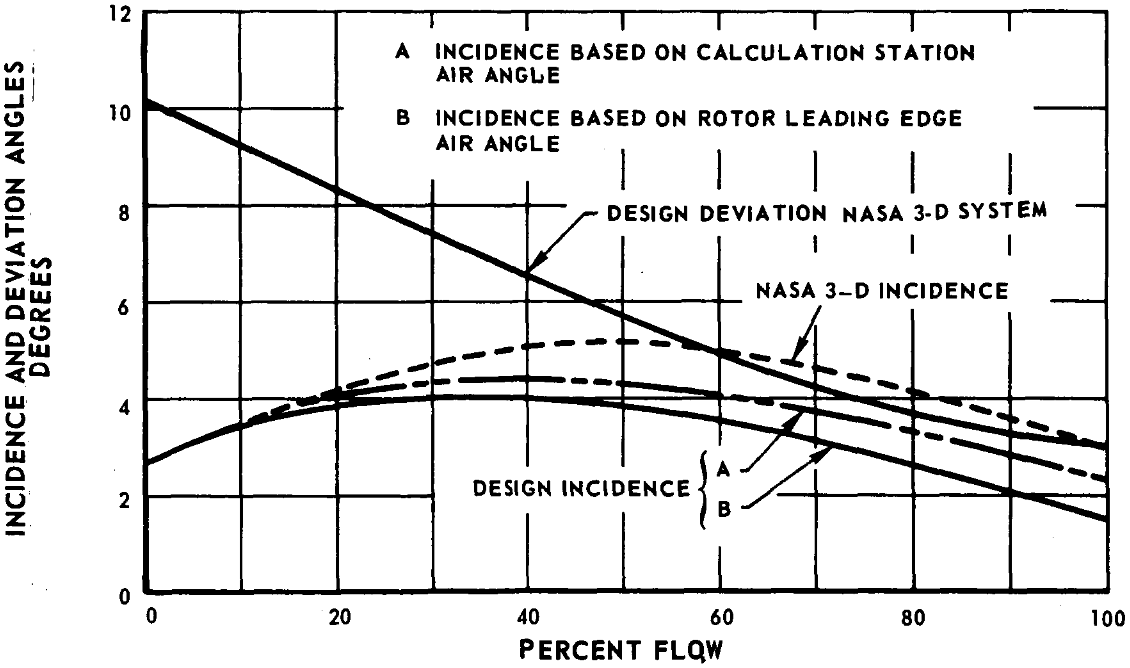

Figure 15 Rotor Incidence and Deviation Angles

3. $\beta_1'^*$ at the intersection of the blade leading edge with a particular streamline was obtained by subtracting the incidence angle on Figure 15 from the β_1' on Figure 11. Similarly, $\beta_2'^*$ at the intersection of a blade trailing edge with a streamline was obtained by subtracting the deviation angle on Figure 15 from the β_2' on Figure 13. Corrections for sweep and dihedral were then calculated, using the method presented in Reference 4. These corrections are tabulated below. Positive terms indicate corrections which increase blade angles.

	hub	mean	tip
Change in leading edge (degrees)	1.1	1.2	0
Change in trailing edge (degrees)	-2.6	-2.0	0

Resulting blade angles are shown as solid lines on Figure 16. The rotor blade is designed so that double-circular-arc sections fall on cylindrical surfaces with blade sections having the $\beta_1'^*$ and $\beta_2'^*$ values from Figure 16.

4. An additional correction was required to compensate for blade untwist produced by centrifugal loading. Static blade angles were set so that the untwist at design speed produces the desired operating blade angles. Resulting static blade angles are shown as dashed lines on Figure 16.

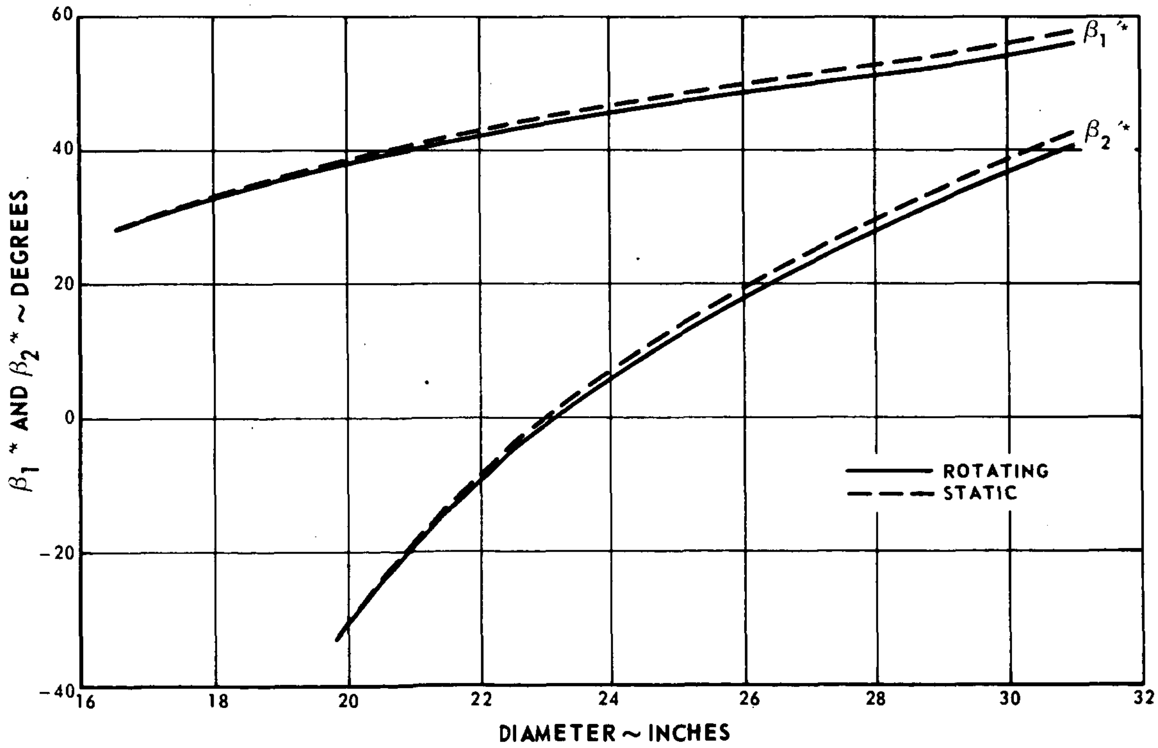

Figure 16 Rotor Metal Angles

The rotor blades were tilted tangentially 0.02 inch to reduce the gas bending stresses. The effect of tilt on the rotor blade stress is shown in Figure 17.

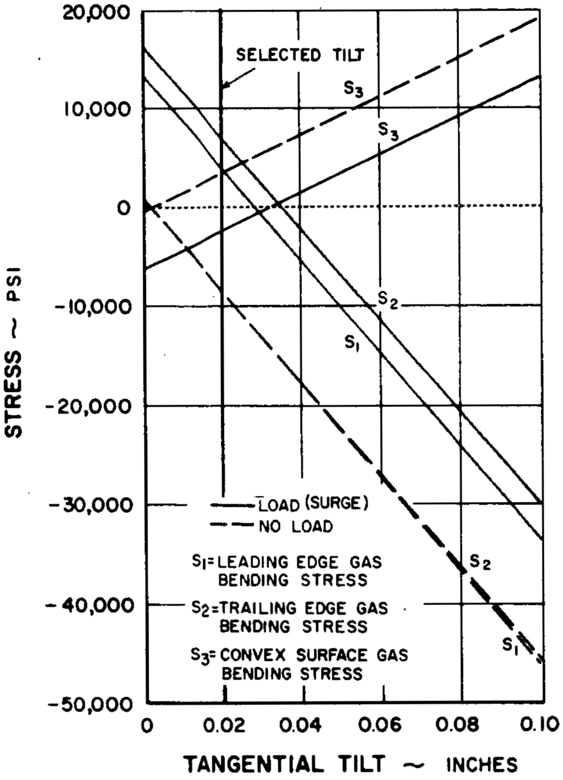

Figure 17 Effect of Tangential Tilt on Rotor Stress

The aerodynamic loading parameter and diffusion factor for the rotor are shown in Figure 18. Both of these parameters are quite low to ensure satisfactory operation. The rotor geometry is summarized in Appendix D.

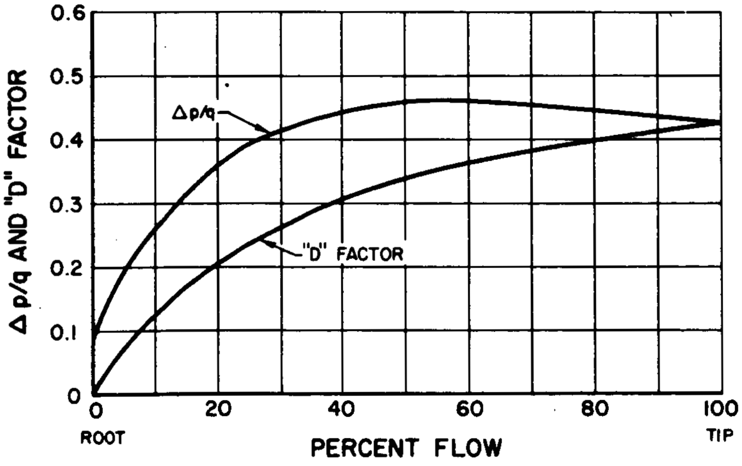

Figure 18 Rotor Aerodynamic Loading and Diffusion Factor

C. Stators

The objective of this investigation is to obtain blade element data on a family of blade shapes which it is thought will be suitable for stator blade sections which operate at high flow Mach numbers. This new family of blade shapes is termed multiple-circular-arc (MCA) blading, defined as two double-circular-arc blades joined at a common transition point. Thus, the forward and rearward portions of the blade are circular-arc sections of different radii. These blade shapes are aimed at controlling the flow turning over the forward portion of the blade with respect to the total turning so as to minimize losses associated with flow shocks. As has been indicated by typical blade surface velocity distributions around compressor blades in cascade, an accelerating flow field exists over the forward portion of the blade suction surface, followed by a decelerating flow field. If the inlet Mach number coupled with the flow turning along the suction surface is sufficiently high, the flow will be accelerated to supersonic velocities as illustrated in figure 19. Figure 19a depicts the flow configuration for high subsonic inlet velocities and figure 19b depicts the flow configuration for supersonic inlet velocities. With supersonic inlet flow a bow wave is formed at the blade leading edge. The flow is decelerated subsonically in passing through the bow wave and is reaccelerated through Mach one on moving around the blade leading edge as indicated by the sonic line. Behind the sonic line is a region where the flow is supersonic. The fluid within the supersonic flow field must be decelerated to the subsonic leaving velocities. This deceleration generally takes place in the form of a normal shock as illustrated in the figure. A loss in total pressure occurs across the shock, and the shock boundary layer interaction can result in increased losses above normal profile losses. The losses associated with the shock can be reduced by reducing the Mach number ahead of the shock and thus the shock strength. This can be accomplished for a given inlet relative Mach number by reducing the flow turning ahead of the shock. However, it is recognized that when the flow turning is reduced in the supersonic flow regime ahead of the shock, it must be increased in the subsonic flow regime behind the shock to obtain the desired total turning of the flow. Increasing the flow turning in the subsonic flow regime will tend to increase the profile losses. Thus a blade turning (loading) distribution which would provide minimum loss would be one that would minimize the sum of the losses from these two sources.

To obtain blade element data on stator blade rows employing the MCA blade shape, two stator blade rows have been designed utilizing this shape. They have been designed for two chordwise distributions of loading. A third stator blade row using double circular arc blades has been designed for the same inlet and outlet flow conditions as the other two stator rows. The stator blade row employing double circular arc blades will be used as a reference or base condition in evaluating the performance of the two stator blade rows employing the MCA blade shapes. The multiple circular arc blade shape is defined in Figure 20. In describing the blade shape, it is assumed that a shock condition exists at the blade passage inlet as shown in Figure 19. The assumed passage shock is located by a line which passes through the leading edge radius of one blade and lies normal to the mean passage camber line. The point where this line intersects the suction surface of the next blade defines the location of the shock on that surface.

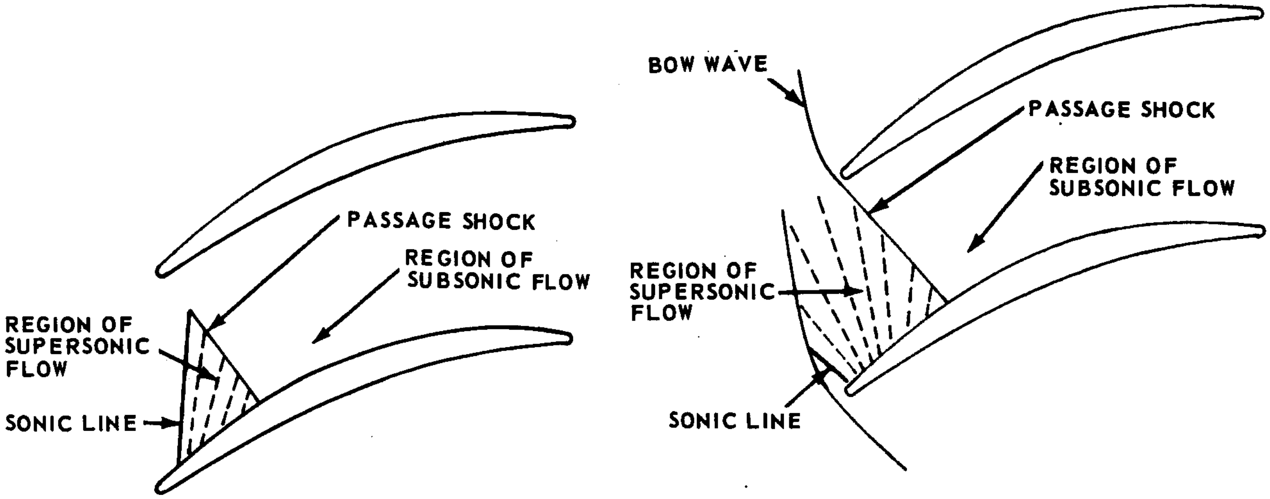

a. HIGH SUBSONIC INLET FLOW

b. SUPERSONIC INLET FLOW

Figure 19 Assumed Blade Passage Flow Configurations

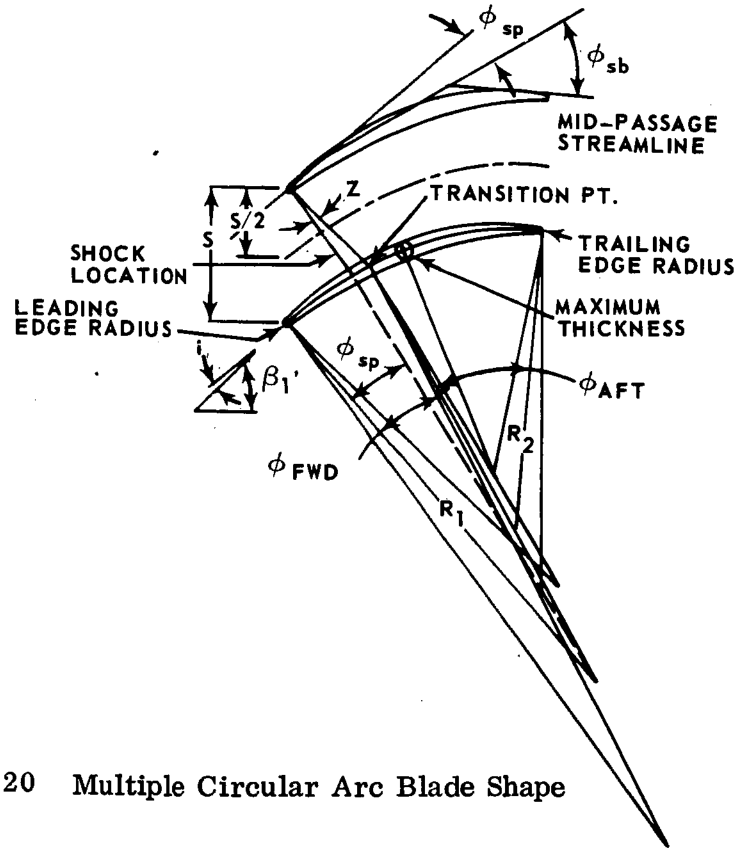

Figure 20 Multiple Circular Arc Blade Shape

In describing the blade shape presented in Figure 20. the subscripts sp and sb are used with reference to the supersonic and subsonic blade shape parameters, respectively. The subscripts fwd and aft are used to define the blade shape parameters for the fore and aft circular arc sections of the blade, respectively. The point where the two circular arc sections are joined is designated as the transition point. The transition point may be at, or related to, the assumed shock location through the angle Zeta, Z.

The front portion of the blade mean camber line is defined by one circular arc section while the rear portion of the blade mean camber line is defined by another circular arc section. The points from which the arcs are struck fall on a common line so that the two circular arc sections are tangent at the point of contact. This is likewise true for the circular arc sections which form the suction and pressure surfaces. When the maximum thickness point is located at the transition point the centers of all the circular arcs fall on a common line which passes through the transition point. The two independent double circular arc sections provide for controlling the amount of supersonic turning relative to the amount of subsonic turning and thus permit optimizing the shock losses with respect to diffusion losses to obtain minimum overall losses.

The first step in the design of the stators was to select a blade solidity, aspect ratio and thickness-to-chord ratio, since these blade parameters, along with the flow parameters, are required to define the MCA blade section; and they are also needed in arriving at blade loading levels, blade element total pressure losses, and deviation angles for both the MCA and DCA stator designs. A hub solidity of 1.91 (based on mean blade spacing) was selected, along with an aspect ratio of 2.06, which resulted in 63 blades having a chord of 2.155 inches. A maximum blade thickness-to-chord ratio was set equal to 0.04 at the hub and 0.08 at the tip with linear variation between the two locations. The incidence angle for all blade sections was set equal to zero on the suction surface, since this value approximates minimum loss incidence for transonic blading. The stator blading was to be designed to turn the flow to the axial direction.

The second step in the design of the stators was to establish the amount of suction surface camber and thus flow turning ahead of the shock for the two stator blade rows employing the MCA blade shapes. With the degree of supersonic turning selected, other blade shape parameters could then be established. The initial intent was to select two levels of supersonic turning as a percentage of that which results from the DCA stator. The transition point was to be placed at the point of shock for both MCA stators. However, initial analysis indicated the maximum reduction in suction surface turning ahead of the shock consistent with flow choking limitations was about 0.6 of the supersonic turning for the DCA stator. In making this analysis, the incidence angle was set equal to zero on the suction surface. A nominal reduction in shock loss was estimated to be about 0.04 for the limited reduction suction surface camber as compared to that for the DCA stator. As previously indicated, the profile losses may tend to increase as a result of the loading being shifted rearward on the blade and thus possibly reducing the indicated gain in total losses as a result of reduced shock loss. Furthermore, it is difficult to measure relatively small differences in losses. Therefore, it was decided not to select two degrees of supersonic suction surface camber for the MCA stators but to set the value for both at 0.6 of that for the DCA stator and to vary the location of the transition point. For the first stator the transition point was located at the shock intersection point and for the second stator the transition point would be moved behind the assumed shock location. Moving the transition point rearward would tend to reduce the effects of shock-boundary layer interaction and the tendency towards flow separation behind the shock by reducing the rate of turning immediately behind the shock. The Z angle for the first stator was zero. For the second set of MCA stators the transition point was moved behind the shock through an angle Z of 12°. The maximum thickness point was located at the transition point for both MCA stators. For purposes of identification, the stator blade row which has the transition point located at the point of shock is designated MCA-A and the stator blade row which has the transition point located behind the passage shock is designated MCA-B.

The supersonic surface camber for the DCA stator and the two MCA stators is presented in Figure 21 as a percent of stator inlet blade height. Figure 22 shows the estimated variation in the suction surface Mach number ahead of the shock as a function of percent stator blade height for all three stators. The variations in stator inlet Mach number are also shown in Figure 22 for comparison with the suction surface Mach number. In the hub region, where the inlet flow was supersonic, the suction surface Mach number was determined from the inlet Mach number and the acceleration resulting from a Prandtl-Meyer expansion based on the turning of the suction surface ahead of the shock. Where the inlet flow dropped below sonic level its value was assumed to be unity so that the Prandtl-Meyer expansion could be used to provide an indication of the Mach number ahead of the shock. In actuality, this method will overestimate the Mach number at the point of shock because some of the so-called supersonic camber on the suction surface will be required to accelerate the flow to sonic conditions and the actual Mach number at the shock on the suction surface will be less than predicted. This method, however, was employed in comparing the MCA stators with the DCA stator and utilized in estimating the shock losses for the blade rows. As indicated in Figure 22, the inlet flow Mach number at the hub was 1.1. The turning on the suction surface accelerated the flow to a Mach number of approximately 1.5 for the MCA stators and to 1.8 for the DCA stator. Similar trends are indicated at the other blade locations.

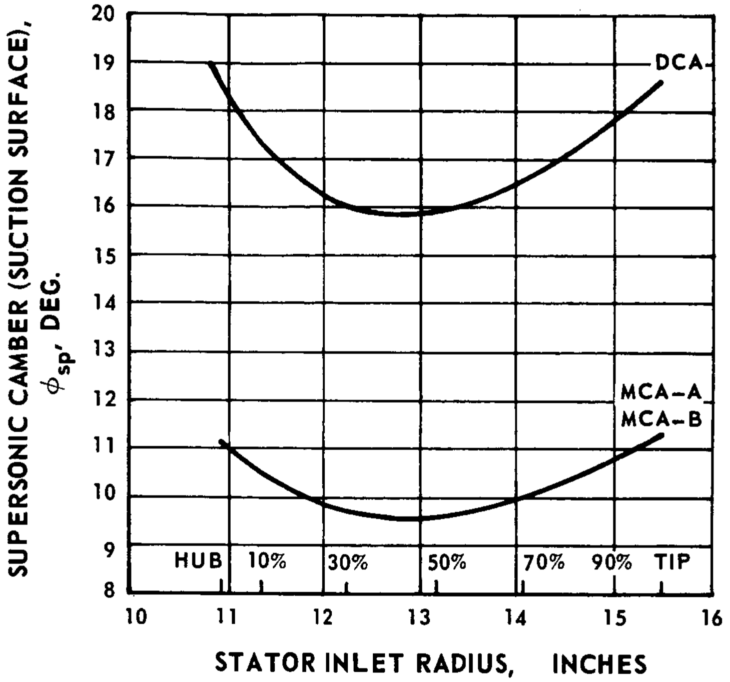

Figure 21 Suction Surface Camber Ahead of the Passage Shock (Supersonic Camber) for the DCA and MCA Stator Blade Rows

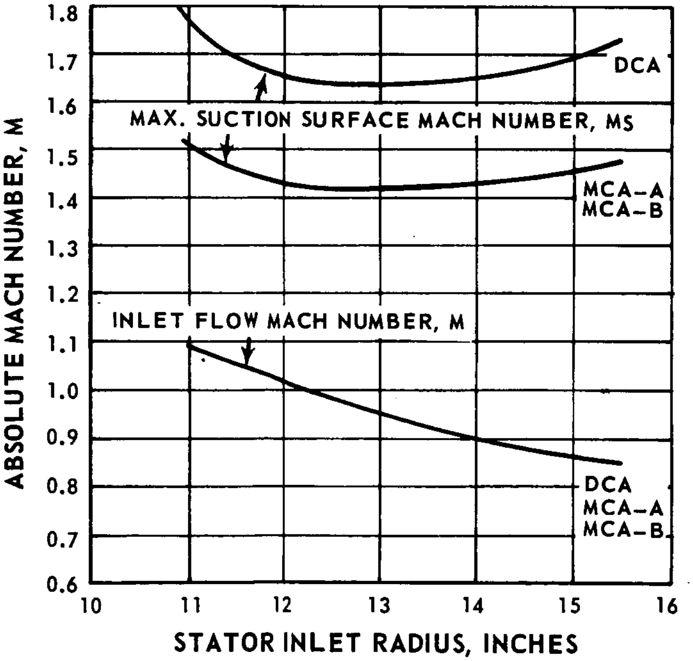

Figure 22 Inlet Flow Mach Number and Estimated Maximum Suction Surface Mach Number for DCA and MCA Stator Blade Rows

Figure 23 shows a comparison of blade area ratio (ratio of upstream capture area to blade throat area) based upon incremental blade height and critical area ratio (ratio of upstream capture area to the area which would result in the flow being accelerated or decelerated to Mach one) as a function of percent of inlet blade height. Two values of critical area ratios are given. One assumes isentropic flow between the inlet area and the throat area and the other takes into account the loss across the passage shock. The passage shock strength was estimated based on an average of the inlet Mach number and the suction surface Mach number indicated in Figure 22. As shown in Figure 23, the DCA stator has greater choke margin than the MCA stators. However, this choke margin for the DCA stator comes at the expense of high shock losses as a result of high suction surface turning. The design objective for the stators employing the MCA blade shape was to minimize the shock losses by setting the suction surface turning ahead of the passage shock at a minimum consistent with the flow choking limitation. For both the MCA stators and the DCA stator the choke margin is larger in the tip region than in the hub region.

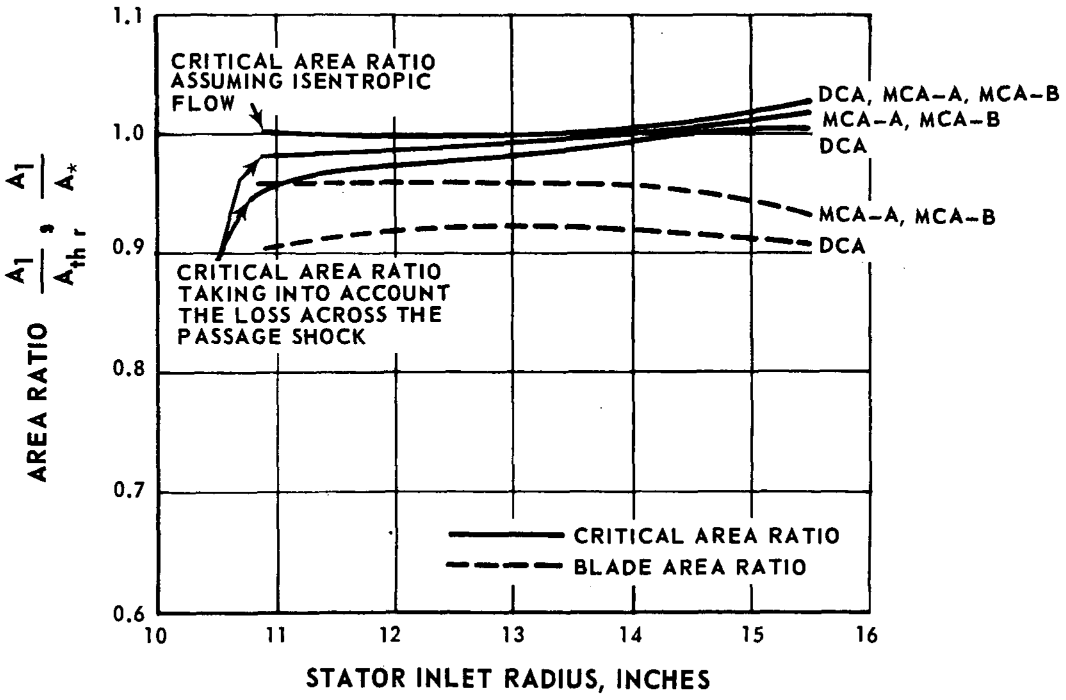

Figure 23 Comparison of Blade Area Ratio with Critical Area Ratio for the Three Sets of Stators

Because blade loading and losses are interrelated it is necessary to perform an iteration in the design to arrive at their respective values. Figure 24 is a plot of diffusion factor as a function of percent of stator inlet blade height. A slightly higher diffusion factor is indicated for the MCA stators as compared to the DCA stator. This is a result of a slight reduction in axial velocity at the stator outlet for the MCA stators related to the lower estimated losses for these stators. The estimated total pressure loss for the stators is given in Figure 25. Where the incoming flow to the stator was supersonic, the method presented in Reference 7 was employed in estimating the total pressure loss across the stator. This method basically calculates a loss across a normal shock based on an average of the inlet and suction surface Mach numbers and adds this value to a profile loss derived from the diffusion factor–loss correlation presented in Reference 8. The method of estimating shock losses presented in Reference 7 was based on supersonic inlet flow and does not include the high subsonic inlet flow condition because of the difficulty in estimating the suction surface Mach number ahead of the shock. For purposes of estimating, the Mach number was assumed unity to permit use of the Prandtl-Meyer expansion. The average of the inlet Mach number and the suction surface Mach number estimated in this manner was used to estimate the shock loss in this region of the blade. The shock loss was assumed the same for the MCA stators since the suction surface turning ahead of the shock was set equal for both blade rows. The profile losses for the MCA stators and the DCA stator were calculated to be essentially of the same magnitude, since their differences in loading level based on blade inlet and outlet conditions were small as indicated by D-factor (Figure 24). The calculated profile loss was approximately 0. 10, 0. 07, and 0. 06 for the hub, mean, and tip sections respectively.

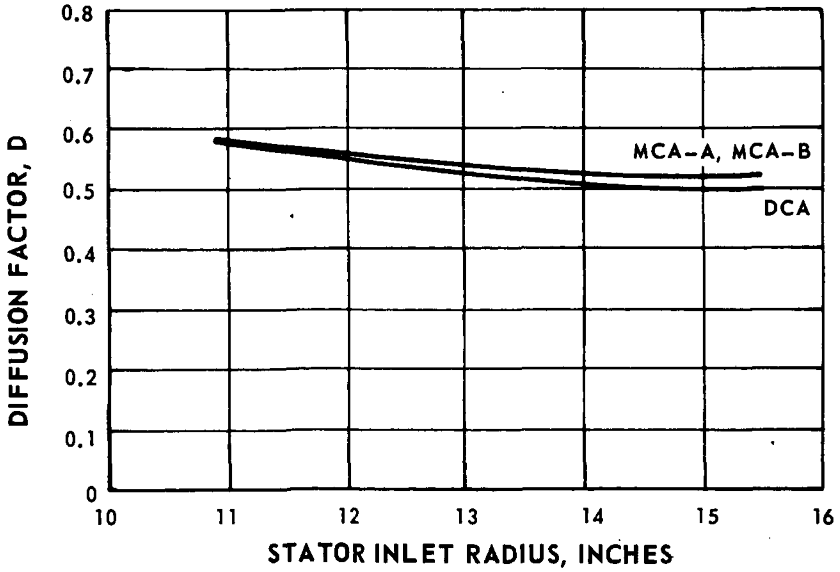

Figure 24 Blade Loading for MCA and DCA Stators

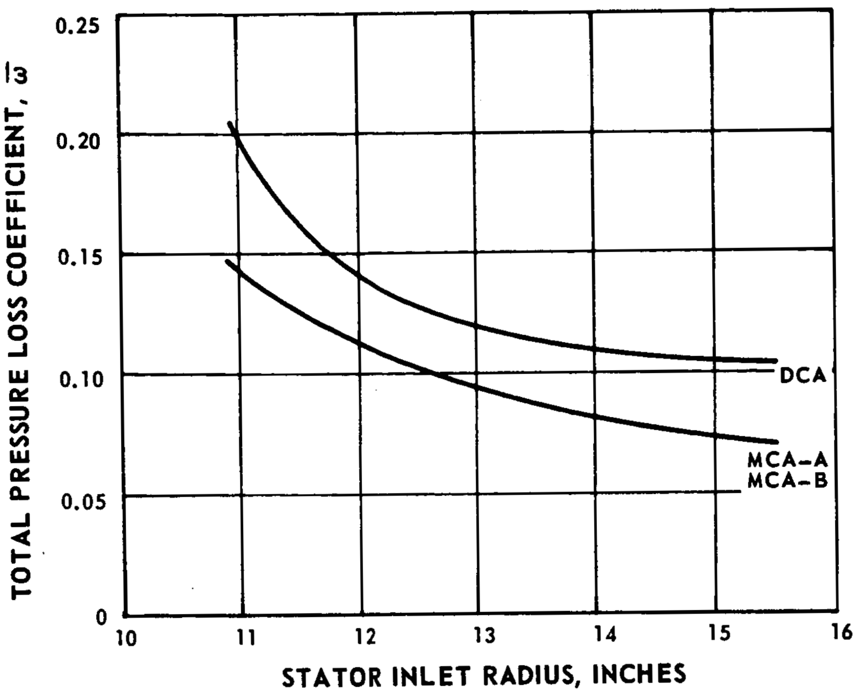

Figure 25 Estimated Total Pressure Loss for MCA and DCA Stators

No attempts were made to estimate the possible increase in profile loss for the MCA stators over the DCA stators or an increase in profile loss for the MCA-B stator over the MCA-A stator as the result of the loading being shifted rearward on the blade. Present loss correlation techniques are not adequate to provide quantitative numbers on profile losses as a function of loading distributions since loading parameters such as D-factor are based upon blade inlet and outlet flow conditions rather than local flow conditions.

Incidence angle based \on the mean camber line is shown in Figure 26 for the three sets of stators. The incidence on the suction surface was set equal to zero for the full blade span. The variation in incidence on the mean between the three blade rows is primarily a result of the difference in the location of blade maximum thickness.

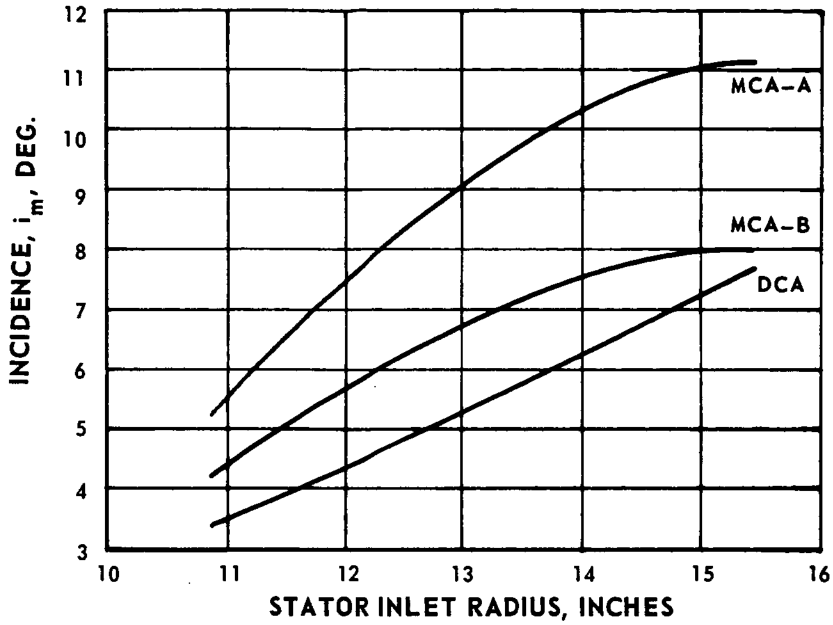

Figure 26 Incidence Angle Based Upon Mean Blade Angle for MCA and DCA Stators

The estimated deviation angle for the three stators is shown in Figure 27. Carter's rule was used in estimating the deviation. It was modified according to Reference 9 to account for changes in camber distribution.

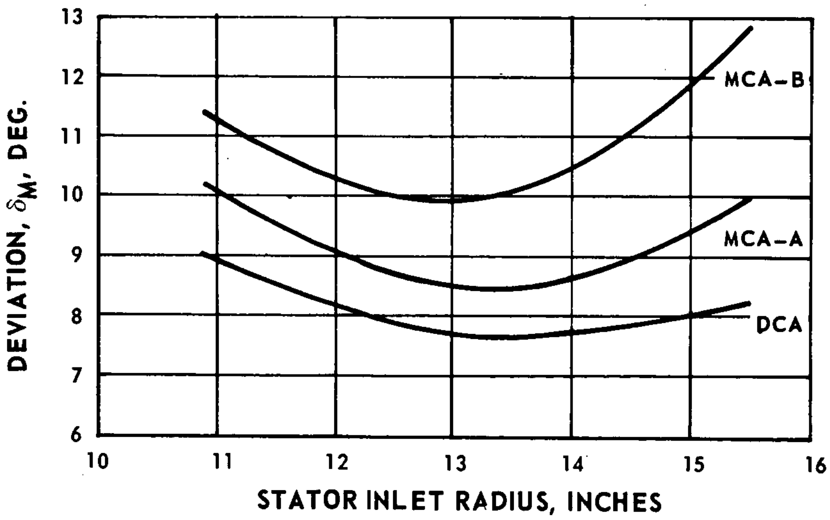

Figure 27 Estimated Deviation Angle for MCA and DCA Stators

Figure 28 is a plot of blade camber angle as a function of blade span for the three stators.

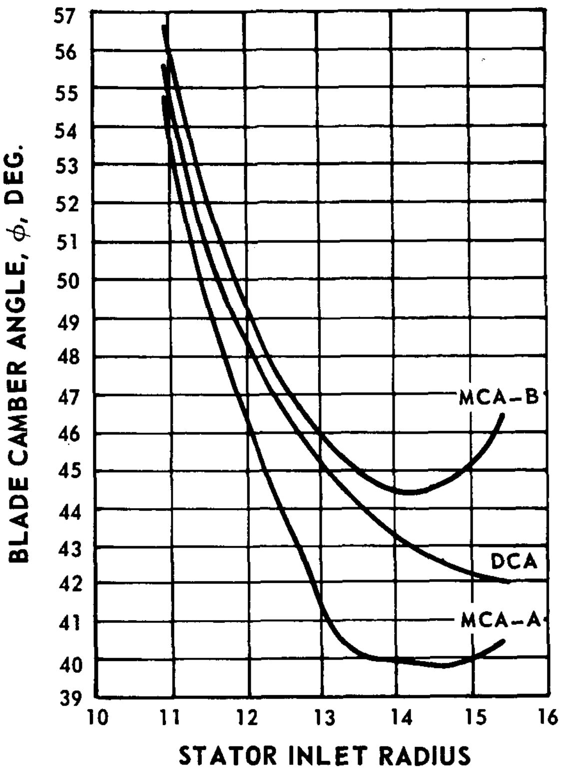

Figure 28 Blade Camber Angle for MCA and DCA Stators

The stator blade rows were designed based on velocities calculated at axial stations which passed through the leading and trailing edge of the stator at the hub location. The blade elements were laid out on conical surfaces approximating the stream surface passing through the blade. The rate of turning of the flow along this surface was set equal to that in a two-dimensional cascade having the blade shapes specified for the DCA and MCA blades. All aerodynamic design data including incidence and deviation were based on velocities and flow angles in the meridional plane, as given in Appendix B. Tabulated values of airfoil design data are presented in Appendix D.

V. STRUCTURAL AND VIBRATION ANALYSIS

A. Blade and Disk Vibration

A blade-disk analysis was performed using the final rotor blade design and a disk which was somewhat lighter than that specified in the present design. The first coupled mode was found to be primarily blade vibration with little disk participation. The resonance diagram (see Figure 29) shows that the 2E (two excitations per revolution) and 3E (three excitations per revolution) resonances occur outside the running range. The 4E resonance occurs at 7650 rpm, but there is nothing in the flow path to excite the blades in a high 4E stress. Excitation could occur from the twelve inlet support struts at 2350 rpm and from the eight exit support struts at 3550 rpm, but both speeds are below the lowest test speed.

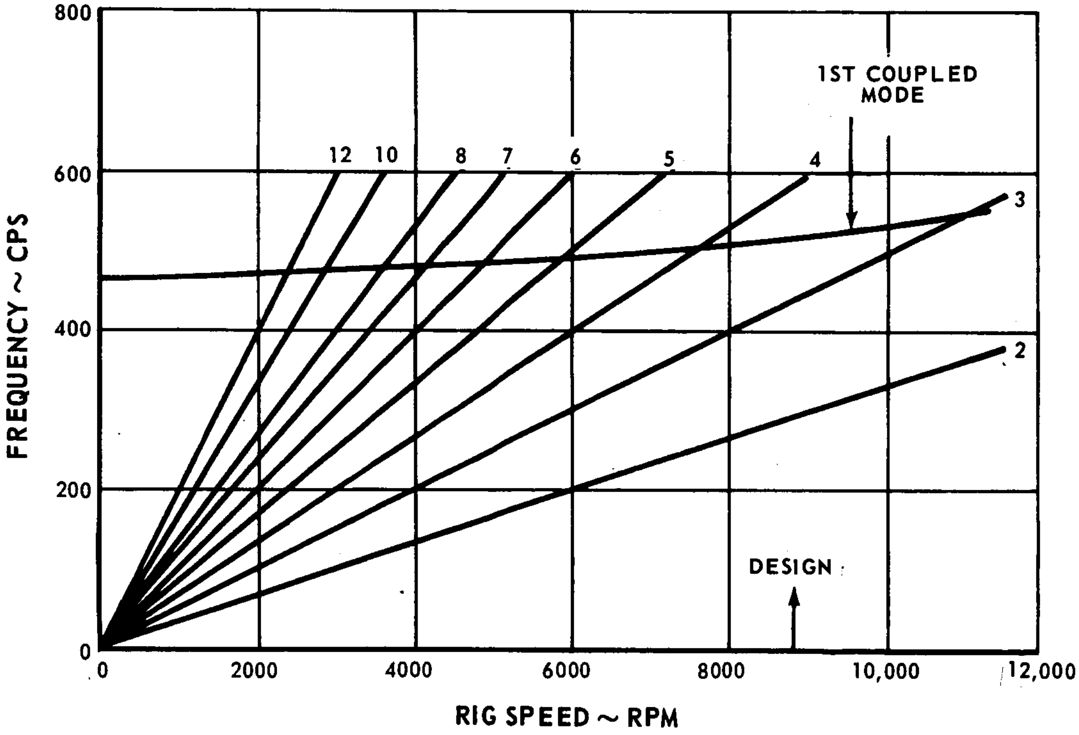

Figure 29 Rotor Resonance Diagram

B. Blade Stress

Properties of the blade material, AMS 4928 titanium alloy, were evaluated at 150°F. Stress Calculations were made for 105 percent of the design speed. Maximum stress at this speed was so low that no problems were anticipated through 110% of design speed.

The maximum centrifugal stress will be 25,000 psi, and the maximum local bending stress at the blade platform due to untwist will be 35,100 psi. The combined stress will be 60,100 psi, which is well below the 100,000 psi stress at which many Pratt & Whitney Aircraft blades operate.

An additional steady stress will be produced by gas bending. The maximum gas bending stress occurs at the trailing edge and has been reduced to 7300 psi by tilting the airfoil tangentially 0.02 inch toward the convex side. This stress does not combine with the maximum centrifugally-induced stress, since the maximum stresses occur at different chord locations.

A Goodman diagram was developed for the blade material at 150°F and is presented in Figure 30. The maximum allowable transient and steady vibratory stresses are 15,000 and 10,000 psi respectively. Since blades were designed for steady vibratory stress less than 5,000 psi, the Goodman diagram indicates that the blades will have adequate fatigue characteristics.

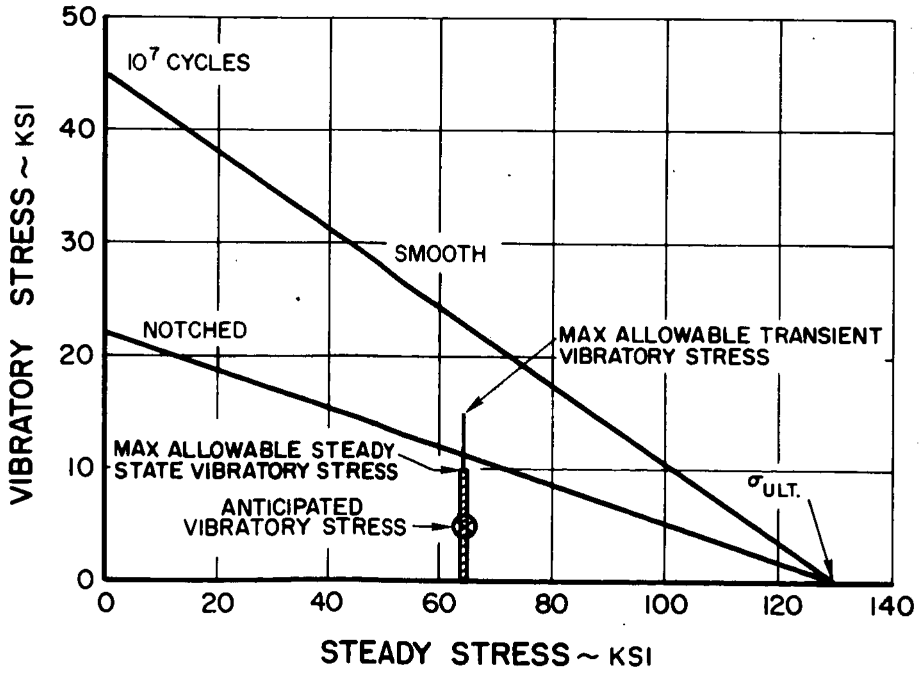

Figure 30 Goodman Diagram for AMS 4928 Titanium Alloy at 150°F

Air loads were calculated for the inlet guide vane, the rotor, and the stator. Gas bending stresses were calculated for the rotor and the stator. Gas bending stresses for the inlet guide vane were not calculated, but they will be insignificant. The NACA double circular arc base point stator with guided cantilever construction was used for the stator calculation. The results are presented in Table I.

TABLE I

AIR LOADS AND GAS BENDING STRESSES

	Inlet Guide Vane	Rotor	Stator
Material	AMS 5613	Titanium	AMS 5613
Number of Airfoils	27	28	63
Axial Load (lb)	46.5	1399	1208
Axial Load Diameter (in.)	23.5	26.27	26.45
Tangential Load (lb)	92.6	1830	2958
Tangential Load Diameter (in.)	23.5	25.20	26.68
Maximum Gas Bending Stress (psi)	-	7300	15259
Root Centrifugal Force (lb)	-	16982	-
Pull per Unit Root Area (lb/in^2)	-	64933	-

Note: Loads are for entire row. Loads for single airfoils are obtained by dividing by the number of airfoils.

C. Blade Torsional Flutter

The torsional flutter parameter, $b\omega_t$ (where b is the blade chord at 75 percent span and ω_t is the torsional frequency) was calculated for the rotor blade. For the rotor blades, the torsional flutter parameter equals 2400. This is well above the level at which flutter problems occur (1000 and below). These blades, therefore, should be free of flutter.

D. Critical Speeds

A critical speed analysis was conducted and the results are presented in Table II. The bearing support spring rates were calculated by using unit radial loads. The longitudinal support structures were applied to the calculation as frame members. Axial load was not considered in calculating the bearing spring rates since experience has shown that applying such a load does not produce nonlinearities.

As shown, the rigid body vibration mode occurs at 3269 rpm, which is below the lowest test speed. The next critical speed occurs at 10,985 rpm, which is 12 percent above the maximum test speed.

TABLE II

CRITICAL SPEED ANALYSIS

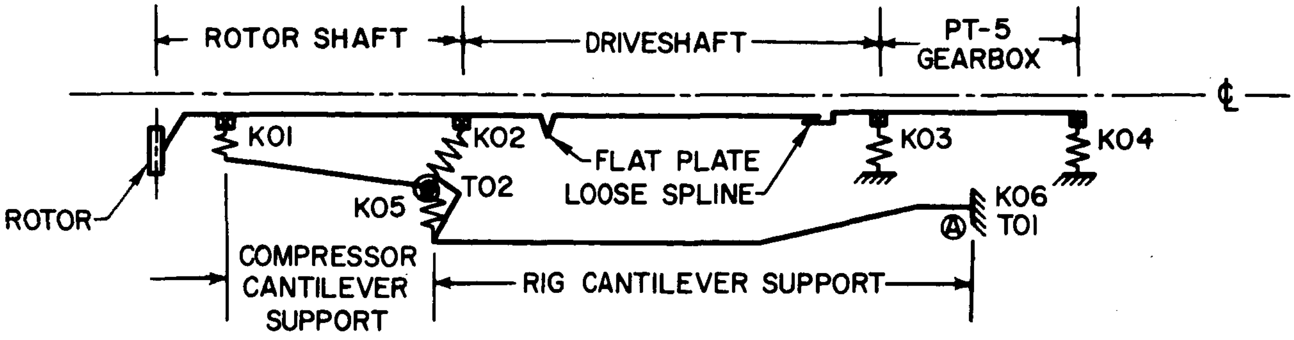

Spring Rates

Linear Constant	Spring Rate(lb/in)	Torsional Constant	Spring Rate(in lb/rad)
KO1	10.74×10^6	TO1	1.00×10^{10}
KO2	11.99×10^6	TO2	854.70×10^{10}
KO3	2.07×10^6		
KO4	2.28×10^6		
KO5	19.98×10^6		
KO6	1.00×10^6		

Critical Speeds

Critical Speed (rpm)	Mode Shape Description
3,269	Conical rigid body mode about cantilever mount
10,985	First rotor critical speed (shaft in bending)
20,984	First driveshaft critical speed (shaft in bending) case out of phase
23,149	Second driveshaft critical speed (shaft in bending) case in phase

APPENDIX A

Nomenclature

NOMENCLATURE

a = partial chord

b = chord at 75% span, inches

c = chord, inches

D = diffusion factor $= 1 - \dfrac{V_{i+1}}{V_i} + \dfrac{r_{i+1}(V_{\theta i+1}) - r_i(V_{\theta i})}{(r+r_{i+1})V_i\sigma}$

i = 1 for rotors and 2 for stators; V_i and V_{i+1} become V_i' and V_{i+1}' respectively for rotors.

M = Mach number

P = total or stagnation pressure, lbs/ft^2

p = static or stream pressure, lbs/ft^2

R, θ, z = cylindrical coordinate system located with z axis as rig center line and with unit vectors $\bar{i}$, $\bar{j}$, and $\bar{k}$ respectively.

S = blade spacing, inches

T = total or stagnation temperature, °R

t = blade maximum thickness, inches

U = rotor speed, ft/sec

V = air velocity, ft/sec

$\bar{V}$ = absolute air velocity vector $= V_R \bar{i} + V_\theta \bar{j} + V_z \bar{k}$, ft/sec

$\bar{V}'$ = relative air velocity vector $= V_R \bar{i} + V_\theta' \bar{j} + V_z \bar{k}$, ft/sec

V_m = meridional air velocity $= (V_R^2 + V_z^2)^{1/2}$, ft/sec

$\bar{X}$ = horizontal distance to airfoil center of gravity from leading edge along chord, inches

$\bar{Y}$ = vertical distance to airfoil center of gravity from chord, inches

Z = Zweiffel Coeff. $= \dfrac{2}{\sigma}\left[\dfrac{\sqrt{V_z^2 + \left(\dfrac{\Delta V_\theta}{2}\right)^2}\;\Delta V_\theta}{V_2^2}\right]$, only for inlet guide vane.

β_z = absolute air angle $= \cot^{-1}(V_z/V_\theta)$, degrees (plane parallel to z axis)

β_m = absolute air angle $= \cot^{-1}(V_m/V_\theta')$ degrees (meridional plane)

β'_z = relative air angle = $\cot^{-1}(V_z/V_\theta')$, degrees

β'_m = relative air angle = $\cot^{-1}(V_m/V_\theta')$, degrees

β^* = blade metal angle for inlet guide vanes, angle between tangent to mean camber line and axial direction on a cylindrical surface at the leading or trailing edge, degrees. For stators, angle between tangent to mean camber line and meridional direction at the leading and trailing edge, degrees.

β'^* = rotor metal angle, angle between tangent to mean camber line and axial direction on a cylindrical surface at the leading or trailing edge, degrees.

γ° = blade-chord angle, angle between blade chord and axial direction on a cylindrical surface, degrees

ϵ = angle between tangent to streamline projected on meridional plane and axial direction, degrees

ρ = density, lbs-sec^2/ft^4

σ = solidity, ratio of chord to spacing

ϕ = blade camber angle, difference between blade angles at leading and trailing edges on a cylindrical surface $\beta_1'^* - \beta_2'^*$ for rotors and $\beta_2^* - \beta_3^*$ for inlet guide vanes, degrees, and on the meridional surface $\beta_2^* - \beta_3^*$ for stators, degrees.

ω = angular velocity of rotor, radians/sec

ω_t = torsional frequency, radians/sec

$\overline{\omega}$ = total pressure loss coefficient, mass averaged defect in relative total pressure divided by the difference between the inlet stagnation and static pressure

$\Delta p/q$ = aerodynamic loading parameter $(p_{i+1} - p_i)/(\rho_i V_i^2/2)$
i=1 for rotors and 2 for stators; V becomes V' for rotors.

Subscripts

r = coordinate normal to axis with unit vector $\bar{i}$
z = coordinate along axis with unit vector $\bar{k}$
θ = coordinate in tangential direction with unit vector $\bar{j}$
1 = station into a rotor
2 = station out of a rotor or into a stator or inlet guide vane
3 = station out of a stator or inlet guide vane

sp = supersonic, portion of blade ahead of assumed passage shock location
sb = subsonic, portion of blade behind assumed passage shock location
fwd = portion of blade ahead of maximum thickness point
aft = portion of blade behind maximum thickness point
m = blade mean surface
s = blade suction surface
mc = portion of blade ahead of maximum camber point

Superscript

' = relative to rotor

APPENDIX B

Aerodynamic Design Data

(See Figure B-1 for Location of Calculation Station)

Instrument Plane Ahead of Inlet Guide Vane Z = -1.2

Percent Flow	0	10	20	30	40	50	60	70	80	90	100
Diameter	16.0	18.1	20.0	21.7	23.2	24.7	26.1	27.4	28.6	29.8	31.0
P	2116.0	2116.0	2116.0	2116.0	2116.0	2116.0	2116.0	2116.0	2116.0	2116.0	2116.0
T	518.6	518.6	518.6	518.6	518.6	518.6	518.6	518.6	518.6	518.6	518.6
M	0.461	0.463	0.466	0.467	0.469	0.470	0.471	0.471	0.471	0.471	0.470
V	505.7	508.0	510.4	512.3	513.7	514.8	515.6	516.0	516.0	515.6	515.2
V_z	505.7	508.0	510.4	512.2	513.7	514.8	515.6	516.0	516.0	515.6	515.2
V_m	505.8	508.0	510.4	512.3	513.7	514.8	515.6	516.0	516.0	515.6	515.2
V_θ	0.0	0.0	0.0	0.0	0.0	0.0	0.0	0.0	0.0	0.0	0.0
β_z	0.0	0.0	0.0	0.0	0.0	0.0	0.0	0.0	0.0	0.0	0.0
ϵ	-0.115	0.085	0.272	0.369	0.391	0.364	0.310	0.246	0.183	0.118	0.056
M_z	0.461	0.463	0.466	0.467	0.469	0.470	0.471	0.471	0.471	0.471	0.470
M_m	0.461	0.463	0.466	0.467	0.469	0.470	0.471	0.471	0.471	0.471	0.470
β_m	0.0	0.0	0.0	0.0	0.0	0.0	0.0	0.0	0.0	0.0	0.0

Inlet Guide Vane Inlet Z = 0.0

Percent Flow	0	10	20	30	40	50	60	70	80	90	100
Diameter	16.0	18.1	20.0	21.7	23.2	24.7	26.1	27.4	28.6	29.8	31.0
P	2116.0	2116.0	2116.0	2116.0	2116.0	2116.0	2116.0	2116.0	2116.0	2116.0	2116.0
T	518.6	518.6	518.6	518.6	518.6	518.6	518.6	518.6	518.6	518.6	518.6
M	0.458	0.460	0.463	0.466	0.469	0.471	0.472	0.473	0.473	0.473	0.472
V	502.7	504.3	507.7	511.0	513.8	516.0	517.5	518.3	518.5	518.0	517.4
V_z	502.7	504.3	507.6	510.9	513.7	515.9	517.5	518.3	518.5	518.0	517.4
V_m	502.7	504.3	507.7	511.0	513.8	516.0	517.5	518.3	518.5	518.0	517.4
V_θ	0.0	0.0	0.0	0.0	0.0	0.0	0.0	0.0	0.0	0.0	0.0
β_z	0.0	0.0	0.0	0.0	0.0	0.0	0.0	0.0	0.0	0.0	0.0
ϵ	0.307	0.633	0.770	0.801	0.750	0.637	0.482	0.298	0.108	-0.044	-0.148
M_z	0.458	0.460	0.463	0.466	0.469	0.471	0.472	0.473	0.473	0.473	0.472
M_m	0.458	0.460	0.463	0.466	0.469	0.471	0.472	0.473	0.473	0.473	0.472
β_m	0.307	0.633	0.770	0.801	0.750	0.637	0.482	0.298	0.108	-0.044	-0.148

Percent Flow	0	10	20	30	40	50	60	70	80	90	100
Inlet Guide Vane Exit Z = 3.0											
Diameter	16.1	18.3	20.2	21.9	23.4	24.8	26.2	27.4	28.6	29.8	30.9
P	2073.7	2090.1	2095.2	2094.8	2094.8	2094.8	2094.8	2095.5	2090.6	2081.3	2073.7
T	518.6	518.6	518.6	518.6	518.6	518.6	518.6	518.6	518.6	518.6	518.6
M	0.598	0.585	0.579	0.574	0.571	0.570	0.568	0.568	0.564	0.567	0.550
V	646.2	633.3	627.3	622.3	619.6	617.9	616.8	615.9	611.8	604.8	598.0
V_z	498.9	520.2	534.7	543.6	551.2	557.5	562.6	566.9	566.7	562.8	558.6
V_m	499.0	520.5	535.3	544.2	551.8	557.9	562.9	567.0	566.8	562.8	558.6
V_θ	410.6	360.9	327.1	301.8	281.9	265.7	252.1	240.5	230.4	221.5	213.4
β	39.5	34.8	31.5	29.0	27.1	25.5	24.1	23.0	22.1	21.5	20.9
ϵ	-0.799	1.865	2.662	2.757	2.529	2.141	1.677	1.180	0.686	0.235	-0.160
M_z	0.461	0.480	0.493	0.501	0.508	0.514	0.519	0.522	0.522	0.518	0.514
M_m	0.461	0.480	0.494	0.502	0.509	0.514	0.519	0.523	0.522	0.518	0.514
β_m	39.5	34.8	31.4	29.0	27.1	25.5	24.1	23.0	22.1	21.5	20.9
Instrument Plane Ahead of Rotor Z = 4.2											
Diameter	16.1	18.4	20.3	22.0	23.5	25.0	26.3	27.5	28.7	29.8	30.9
P	2073.7	2090.1	2095.2	2094.8	2094.8	2094.8	2094.8	2095.5	2090.6	2081.3	2073.7
T	518.6	518.6	518.6	518.6	518.6	518.6	518.6	518.6	518.6	518.6	518.6
M	0.568	0.566	0.571	0.573	0.576	0.578	0.579	0.580	0.577	0.570	0.563
M'	0.467	0.563	0.646	0.715	0.777	0.832	0.883	0.931	0.973	1.011	1.048
V	616.7	614.1	619.1	621.7	624.3	626.4	627.7	628.4	625.2	618.5	611.6
V'	506.4	611.0	700.7	775.4	842.0	902.2	957.3	1008.5	1054.7	1097.1	1138.2
V_z	459.7	496.9	525.2	542.9	556.5	566.8	574.6	580.5	581.2	577.5	573.1
V_m	460.2	498.5	527.1	544.6	557.8	567.8	575.3	580.8	581.3	577.5	573.1
V_θ	410.6	358.7	324.8	299.8	280.4	264.5	251.3	239.9	230.1	221.3	213.4
V'_θ	-211.4	-353.4	-461.7	-552.0	-630.7	-701.1	-765.2	-824.5	-880.0	-932.8	-983.4
β_z	41.8	35.9	31.7	28.9	26.7	25.0	23.6	22.5	21.6	21.0	20.4
β_z'	24.7	35.4	41.3	45.5	48.6	51.0	53.1	54.9	56.6	58.2	59.8
ϵ	2.539	4.501	4.828	4.534	3.980	3.321	2.633	1.959	1.314	0.688	0.083
U	622.0	712.1	786.4	851.8	911.0	965.6	1016.5	1064.5	1110.1	1154.1	1196.8
M_m	0.424	0.459	0.485	0.502	0.514	0.523	0.530	0.535	0.536	0.532	0.527
M_z	0.423	0.457	0.484	0.500	0.513	0.522	0.530	0.535	0.536	0.532	0.527
β_m	41.7	35.7	31.7	28.8	26.7	25.0	23.6	22.4	21.6	21.0	20.4
β_m'	24.7	35.3	41.2	45.4	48.5	51.0	53.1	54.8	56.6	58.2	59.8

Percent Flow	0	10	20	30	40	50	60	70	80	90	100
Rotor Inlet Z = 6.0											
Diameter	16.6	18.9	20.8	22.4	23.9	25.2	26.5	27.7	28.8	29.9	30.9
P	2073.7	2090.1	2095.2	2094.8	2094.8	2094.8	2094.8	2095.5	2090.6	2081.3	2073.7
T	518.6	518.6	518.6	518.6	518.6	518.6	518.6	518.6	518.6	518.6	518.6
M	0.542	0.562	0.580	0.592	0.601	0.608	0.612	0.615	0.613	0.607	0.600
M'	0.459	0.582	0.674	0.747	0.810	0.866	0.916	0.961	1.001	1.037	1.071
V'	499.9	631.9	730.3	808.5	875.8	935.2	988.6	1037.5	1080.9	1120.4	1158.6
V_z	422.7	489.4	533.3	562.0	583.4	599.1	610.5	618.4	620.2	616.9	612.4
V_m	435.5	501.3	542.9	569.1	588.3	602.3	612.4	619.4	620.6	617.0	612.4
V'_θ	397.3	348.4	317.1	294.1	276.2	261.5	249.1	238.5	229.2	220.9	213.4
β_z	43.2	35.4	30.7	27.6	25.3	23.6	22.2	21.1	20.3	19.7	19.2
β_z'	30.1	38.2	42.5	45.6	48.0	50.0	51.8	52.4	55.0	55.6	58.1
ϵ	13.904	12.525	10.762	9.043	7.416	5.903	4.511	3.237	2.069	0.965	-0.082
U	642.9	733.2	805.5	868.4	924.9	976.8	1025.2	1070.8	1114.3	1156.2	1196.9
M_m	0.400	0.461	0.501	0.525	0.544	0.557	0.567	0.573	0.574	0.570	0.566
M_z	0.388	0.450	0.492	0.519	0.539	0.554	0.565	0.572	0.574	0.570	0.566
β_m	42.4	34.8	30.3	27.3	25.1	23.5	22.1	22.1	20.3	19.7	19.2
β_m'	29.4	37.5	42.0	45.3	47.8	50.0	51.7	53.3	55.0	56.6	58.1
Rotor Exit Z = 10.3											
Diameter	20.3	21.9	23.2	24.3	25.4	26.4	27.4	28.3	29.2	30.1	30.9
P	3279.8	3279.8	3279.8	3279.8	3279.8	3279.8	3279.8	3279.8	3279.8	3279.8	3279.8
T	600.0	595.8	594.9	595.0	594.9	595.7	596.6	598.0	599.7	601.5	604.0
M	1.011	0.963	0.929	0.901	0.877	0.856	0.838	0.822	0.808	0.794	0.782
M'	0.554	0.585	0.603	0.619	0.639	0.656	0.675	0.692	0.708	0.724	0.736
V'	606.5	643.2	666.7	687.2	712.1	734.6	757.9	779.4	800.1	821.1	838.4
V_z	510.1	595.5	627.8	641.4	649.3	650.9	649.8	645.8	640.0	633.3	623.6
V_m	586.4	643.2	657.9	660.4	661.3	658.2	654.1	648.1	641.0	633.6	623.6
V'_θ	155.0	-3.5	-107.5	-190.2	-264.0	-326.0	-382.8	-432.9	-478.9	-522.3	-560.3
β_z	61.5	54.7	51.5	49.5	47.9	46.9	46.2	45.7	45.5	45.4	45.6
β_z'	-16.9	0.3	9.7	16.5	22.1	26.6	30.5	33.8	36.8	39.5	41.9
ϵ	29.546	22.210	17.410	13.797	10.937	8.581	6.570	4.809	3.226	1.774	0.421
U	784.8	846.1	896.6	941.8	983.5	1022.6	1059.8	1095.5	1130.1	1163.7	1196.6
M_m	0.534	0.583	0.594	0.594	0.593	0.588	0.582	0.575	0.566	0.588	0.547
M_z	0.464	0.540	0.567	0.577	0.582	0.581	0.578	0.573	0.565	0.558	0.547
β_m	38.0	52.6	50.2	48.7	47.4	46.4	46.0	45.6	45.5	45.4	45.6
β_m'	-14.8	0.3	9.3	16.1	21.8	26.4	30.4	33.7	36.8	39.5	41.9

Instrument Plane Ahead of Stator Z = 11.05

Double Circular Arc Stator Loss

Percent Flow	0	10	20	30	40	50	60	70	80	90	100
Diameter	21.1	22.5	23.6	24.7	25.7	26.6	27.6	28.4	29.3	30.1	30.9
P	3279.8	3279.8	3279.8	3279.8	3279.8	3279.8	3279.8	3279.8	3279.8	3279.8	3279.8
T	600.0	595.8	594.9	595.0	594.9	595.7	596.6	598.0	599.7	601.5	604.0
M	1.041	1.002	0.965	0.935	0.909	0.887	0.868	0.851	0.836	0.822	0.809
M'	0.634	0.665	0.673	0.679	0.692	0.704	0.717	0.730	0.742	0.755	0.765
V	1134.0	1095.4	1061.2	1032.6	1007.9	987.9	970.1	954.9	941.4	928.8	917.9
V'	691.5	727.5	739.4	750.6	767.5	783.8	801.8	818.9	835.9	853.3	867.7
V_z	612.0	682.1	699.1	702.5	703.1	699.6	694.9	688.4	680.7	672.5	661.9
V_m	686.1	725.9	726.0	719.3	713.6	706.1	698.7	690.4	681.6	672.7	661.9
V_θ	902.9	820.4	773.9	740.9	711.7	690.9	672.9	659.8	649.4	640.5	636.0
V_θ'	86.0	-48.6	-140.2	-214.7	-282.6	-340.2	-393.4	-440.5	-483.9	-525.0	-561.0
β_z	55.9	50.3	47.9	46.5	45.4	44.6	44.1	43.8	43.6	43.6	43.9
β_z'	-8.0	04.1	11.3	17.0	21.9	25.9	29.5	32.6	35.4	38.0	40.3
ϵ	26.868	20.005	15.653	12.416	9.872	7.775	5.973	4.376	2.913	1.552	0.257
U	816.9	869.0	914.1	955.6	994.3	1031.1	1066.3	1100.3	1133.3	1165.5	1197.0
M_m	0.629	0.664	0.660	0.651	0.643	0.633	0.624	0.614	0.604	0.594	0.582
M_z	0.561	0.624	0.636	0.636	0.633	0.627	0.621	0.613	0.603	0.594	0.582
β_m	52.7	48.5	46.8	45.8	44.9	44.4	43.9	43.7	43.6	43.6	43.9
β_m'	-7.1	3.8	10.9	16.6	21.6	25.7	29.4	32.5	35.4	38.0	40.3

Stator Inlet Z = 11.8

Double Circular Arc Stator Loss

Percent Flow	0	10	20	30	40	50	60	70	80	90	100
Diameter	21.8	22.9	24.0	25.0	25.9	26.8	27.7	28.5	29.4	30.1	30.9
P	3279.8	3279.8	3279.8	3279.8	3279.8	3279.8	3279.8	3279.8	3279.8	3279.8	3279.8
T	600.0	595.8	594.9	595.0	594.9	595.7	596.6	598.0	599.7	601.5	604.0
M	1.110	1.053	1.009	0.974	0.945	0.921	0.901	0.884	0.868	0.855	0.842
V	1195.3	1141.3	1101.0	1069.0	1042.1	1020.8	1002.3	986.9	973.5	961.4	951.3
V_z	759.5	779.4	775.2	766.5	759.4	751.0	743.1	734.6	726.0	717.5	707.4
V_m	813.8	811.0	794.9	779.0	767.3	755.8	745.9	736.0	726.6	717.7	707.4
V_θ	875.6	803.1	761.8	732.0	705.2	686.1	669.5	657.4	647.9	639.8	636.0
β_z	49.1	45.9	44.5	43.7	42.9	42.4	42.0	41.8	41.7	41.7	42.0
ϵ	21.042	16.061	12.779	10.259	8.226	6.511	5.001	3.629	2.331	1.073	-0.1904
M_m	0.756	0.748	0.728	0.709	0.695	0.682	0.670	0.659	0.648	0.637	0.626
M_z	0.705	0.719	0.710	0.698	0.688	0.677	0.668	0.657	0.647	0.637	0.626
β_m	47.1	44.7	43.7	43.2	42.6	42.3	41.9	41.8	41.8	41.8	42.0

Stator Exit Z = 14.0

Double Circular Arc Stator Loss

Percent Flow	0	10	20	30	40	50	60	70	80	90	100
Diameter	22.8	23.7	24.7	25.5	26.4	27.2	28.0	28.7	29.5	30.2	30.9
P	2935.4	3005.7	3051.2	3080.4	3100.5	3115.5	3126.2	3134.1	3140.3	3145.9	3151.9
T	600.0	595.8	594.9	595.0	594.9	595.7	596.6	598.0	599.7	601.5	604.0
M	0.610	0.607	0.604	0.601	0.598	0.596	0.594	0.593	0.593	0.594	0.596
V	707.8	701.5	698.5	695.1	691.9	689.9	688.5	688.1	688.8	691.0	694.8
V_z	706.9	700.4	697.3	694.1	691.1	689.3	688.1	687.8	688.7	690.9	694.8
V_m	707.8	701.5	698.5	695.1	691.9	689.9	688.5	688.1	688.8	690.9	694.8
V_θ	0.0	0.0	0.0	0.0	0.0	0.0	0.0	0.0	0.0	0.0	0.0
β_z	0.0	0.0	0.0	0.0	0.0	0.0	0.0	0.0	0.0	0.0	0.0
ϵ	2.837	3.315	3.303	3.063	2.722	2.334	1.922	1.504	1.085	0.675	0.274
M_m	0.610	0.606	0.604	0.601	0.598	0.595	0.594	0.592	0.592	0.593	0.595
M_z	0.609	0.605	0.603	0.600	0.597	0.595	0.593	0.592	0.592	0.593	0.595
β_m	0.0	0.0	0.0	0.0	0.0	0.0	0.0	0.0	0.0	0.0	0.0

Instrument Plane Downstream of Stator Z = 14.9

Double Circular Arc Stator Loss

Percent Flow	0	10	20	30	40	50	60	70	80	90	100
Diameter	22.8	23.8	24.7	25.6	26.4	27.2	28.0	28.8	29.5	30.2	30.9
P	2935.4	3005.7	3051.2	3080.4	3100.5	3115.5	3126.2	3134.1	3140.3	3145.9	3151.9
T	600.0	595.8	594.9	595.0	594.9	595.7	596.6	598.0	599.7	601.5	604.0
M	0.555	0.580	0.592	0.598	0.601	0.602	0.603	0.603	0.603	0.604	0.605
V	648.1	673.2	685.7	691.9	694.9	696.9	698.1	699.1	700.4	702.1	705.0
V_z	648.0	673.1	685.6	691.8	694.8	696.8	698.0	699.1	700.3	702.0	705.0
V_m	648.1	673.2	685.7	691.9	694.9	696.9	698.1	699.1	700.4	702.1	705.0
V_θ	0.0	0.0	0.0	0.0	0.0	0.0	0.0	0.0	0.0	0.0	0.0
β_z,	0.0	0.0	0.0	0.0	0.0	0.0	0.0	0.0	0.0	0.0	0.0
ϵ	- 0.846	0.395	0.954	1.173	1.200	1.115	0.968	0.787	0.597	0.415	0.260
M_m	0.555	0.580	0.592	0.598	0.600	0.602	0.602	0.603	0.603	0.603	0.605
M_z	0.555	0.580	0.592	0.597	0.600	0.602	0.602	0.603	0.603	0.603	0.605
β_m	0.0	0.0	0.0	0.0	0.0	0.0	0.0	0.0	0.0	0.0	0.0

Instrument Plane Ahead of Stator Z = 11.05

Multiple Circular Arc Stator Loss

Percent Flow	0	10	20	30	40	50	60	70	80	90	100
Diameter	21.1	22.5	23.6	24.7	25.7	26.6	27.6	28.4	29.3	30.1	30.9
P	3279.8	3279.8	3279.8	3279.8	3279.8	3279.8	3279.8	3279.8	3279.8	3279.8	3279.8
T	600.0	595.8	594.9	595.0	594.9	595.7	596.6	598.0	599.7	601.5	604.0
M	1.041	1.002	0.966	0.935	0.909	0.887	0.867	0.851	0.835	0.821	0.808
M'	0.634	0.666	0.673	0.680	0.692	0.703	0.717	0.729	0.742	0.754	0.764
V	1134.0	1095.6	1061.3	1032.7	1007.9	987.7	969.8	954.7	941.1	928.5	917.6
V'	691.5	727.8	739.7	750.7	767.5	783.5	801.5	818.5	835.5	852.9	867.3
V_z	612.0	682.4	699.5	702.7	703.2	699.5	694.6	688.0	680.2	672.0	661.4
V_m	686.1	726.0	726.3	719.4	713.6	705.9	698.4	689.9	681.1	672.2	661.4
V_θ	902.9	820.4	773.9	740.9	711.8	690.9	673.0	659.8	649.4	640.5	636.0
V_θ'	86.0	-48.6	-140.2	-214.6	-282.5	-340.1	-393.3	-440.4	-483.9	-525.0	-561.0
β_z	55.9	50.2	47.9	46.5	45.3	44.6	44.1	43.8	43.7	43.6	43.9
β_z'	-8.0	4.1	11.3	17.0	21.9	25.9	29.5	32.6	35.4	38.0	40.3
ϵ	26.868	19.977	15.605	12.357	98.10	7.717	5.923	4.337	2.887	1.539	0.257
U	816.9	869.0	914.1	955.5	994.3	1031.0	1066.3	1100.2	1133.3	1165.4	1197.0
M_m	0.629	0.664	0.660	0.651	0.643	0.633	0.624	0.614	0.604	0.594	0.582
M_z	0.561	0.624	0.636	0.636	0.633	0.627	0.621	0.613	0.603	0.594	0.582
β_m	52.7	48.5	46.8	45.8	44.9	44.4	43.9	43.7	43.6	43.6	43.9
β_m'	-7.1	3.8	10.9	16.6	21.6	25.7	29.4	32.5	35.4	38.0	40.3

Stator Inlet Z = 11.8

Multiple Circular Arc Stator Loss

Percent Flow	0	10	20	30	40	50	60	70	80	90	100
Diameter	21.8	22.9	24.0	25.0	25.9	26.8	27.7	28.5	29.4	30.1	30.9
P	3279.8	3279.8	3279.8	3279.8	3279.8	3279.8	3279.8	3279.8	3279.8	3279.8	3279.8
T	600.0	595.8	594.9	595.0	594.9	595.7	596.6	598.0	599.7	601.5	604.0
M	1.111	1.054	1.001	0.974	0.945	0.921	0.901	0.883	0.868	0.854	0.842
V	1168.4	1142.5	1101.8	1069.3	1042.1	1020.5	1001.8	986.2	972.8	960.7	950.5
V_z	760.6	781.2	776.6	767.2	759.5	750.6	742.4	733.7	725.0	716.5	706.4
V_m	814.9	812.6	796.0	779.4	767.2	755.4	745.2	735.2	725.6	716.6	706.4
V	875.5	803.1	761.8	732.1	705.3	686.1	669.5	657.4	647.9	639.8	636.0
β_z	49.0	45.8	44.4	43.7	42.9	42.4	42.0	41.9	41.8	41.8	42.0
ϵ	21.042	15.986	12.671	10.145	8.124	6.426	4.935	3.582	2.302	1.059	-0.190
M_m	0.757	0.750	0.729	0.710	0.695	0.681	0.669	0.658	0.647	0.636	0.625
M_z	0.706	0.721	0.711	0.698	0.688	0.677	0.667	0.657	0.646	0.636	0.625
β_m	47.1	44.7	43.8	43.2	42.6	42.2	41.9	41.8	41.7	41.7	42.0

Stator Exit Z = 14.0

Multiple Circular Arc Stator Loss

Percent Flow	0	10	20	30	40	50	60	70	80	90	100
Diameter	22.8	23.7	24.6	25.5	26.4	27.2	28.0	28.7	29.5	30.2	30.9
P	3024.9	3069.7	3102.2	3126.0	3143.8	3157.5	3168.1	3176.3	3183.0	3188.7	3193.9
T	600.0	595.8	594.9	595.0	594.9	595.7	596.6	598.0	599.7	601.5	604.0
M	0.609	0.596	0.589	0.585	0.581	0.579	0.578	0.577	0.577	0.578	0.580
V	706.2	689.9	682.2	677.3	673.8	671.8	670.8	670.8	671.8	674.0	677.6
V_z	705.4	688.8	681.2	676.4	673.1	671.3	670.4	670.6	671.7	674.0	677.6
V_m	706.2	689.9	682.2	677.3	673.8	671.8	670.8	670.8	671.8	674.0	677.6
V_θ	0.0	0.0	0.0	0.0	0.0	0.0	0.0	0.0	0.0	0.0	0.0
β_z	0.0	0.0	0.0	0.0	0.0	0.0	0.0	0.0	0.0	0.0	0.0
ϵ	2.837	3.315	3.303	3.063	2.722	2.334	1.922	1.504	1.085	0.675	0.274
M_m	0.608	0.595	0.589	0.584	0.581	0.579	0.577	0.577	0.577	0.578	0.580
M_z	0.607	0.594	0.588	0.583	0.580	0.578	0.577	0.576	0.577	0.578	0.580
β_m	0.0	0.0	0.0	0.0	0.0	0.0	0.0	0.0	0.0	0.0	0.0

Instrument Plane Downstream of Stator Z = 14.9

Multiple Circular Arc Stator Loss

Percent Flow	0	10	20	30	40	50	60	70	80	90	100
Diameter	22.8	23.8	24.7	25.6	26.4	27.2	28.0	28.8	29.5	30.2	30.9
P	3024.9	3069.7	3102.2	3126.0	3143.8	3157.5	3168.1	3176.3	3183.0	3188.7	3193.9
T	600.0	595.8	594.9	595.0	595.0	595.7	596.6	598.0	599.7	601.5	604.0
M	0.557	0.571	0.578	0.581	0.584	0.585	0.586	0.586	0.587	0.588	0.589
V	649.5	662.5	669.7	673.9	676.3	678.1	679.5	680.8	682.4	684.2	686.8
V_z	649.4	662.5	669.6	673.8	676.2	678.0	679.4	680.8	682.3	684.1	686.8
V_m	649.5	662.5	669.7	673.9	676.3	678.1	679.5	680.8	682.4	684.2	686.8
V_θ	0.0	0.0	0.0	0.0	0.0	0.0	0.0	0.0	0.0	0.0	0.0
β_z	0.0	0.0	0.0	0.0	0.0	0.0	0.0	0.0	0.0	0.0	0.0
ϵ	-0.846	0.359	0.924	1.150	1.180	1.098	0.952	0.774	0.588	0.410	0.260
M_m	0.556	0.570	0.577	0.581	0.583	0.584	0.585	0.586	0.586	0.587	0.588
M_z	0.556	0.570	0.577	0.581	0.583	0.584	0.585	0.586	0.586	0.587	0.588
β_m	0.0	0.0	0.0	0.0	0.0	0.0	0.0	0.0	0.0	0.0	0.0

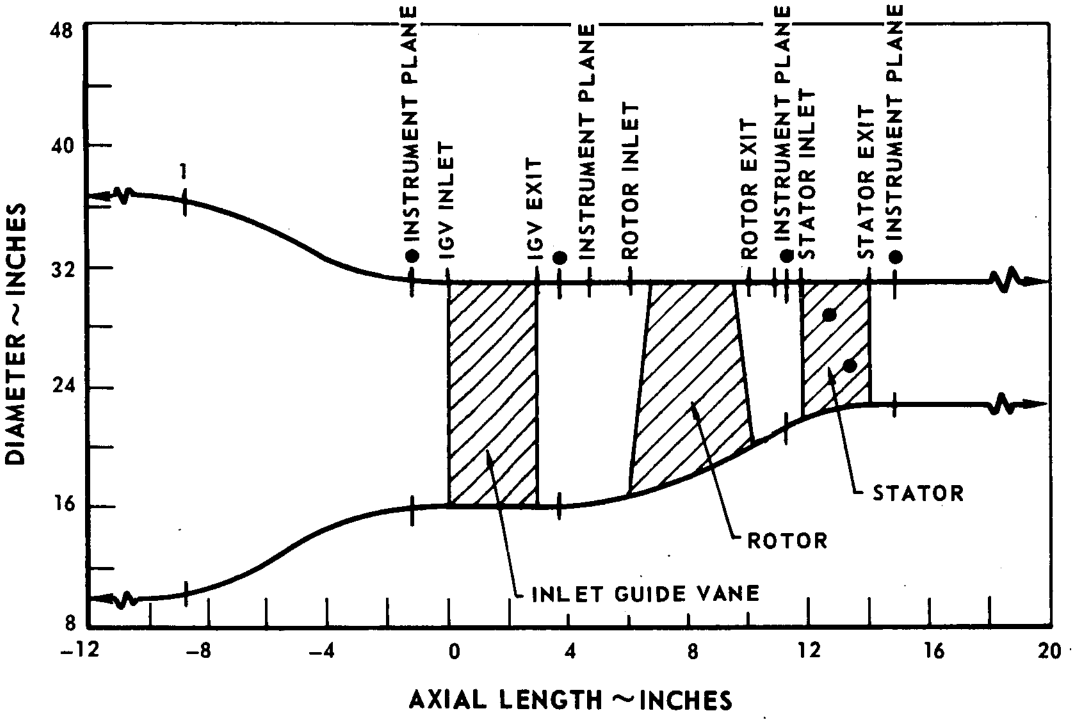

Figure B-1 Calculation Station Locations

APPENDIX C

Inlet Guide Vane Secondary Flow Calculations

INLET GUIDE VANE SECONDARY FLOW CALCULATIONS

The effects of secondary flow were calculated for the inlet guide vane by using the method described by Lieblein et al[2]. The method is divided into four parts.

First, the aerodynamic station air angle is converted to the vane exit. This conversion generally requires correction for sweep and dihedral effects, translation from the aerodynamic calculation station to the vane trailing edge, and compensation for wake effects. The vane, however, has a constant inner and outer diameter and essentially a constant chord. Thus, sweep and dihedral have no effect. Further, the aerodynamic calculation stations are located at the inlet guide vane inlet and exit, and a blockage coefficient is used which simulates the vane wake effects. Consequently, no conversion is required for the data appearing in Appendix B.

The second step involves the calculation of the inlet guide vane exit circulation and velocity. Since the inlet guide vane has a free vortex design, the circulation is constant from root to tip (at 66.0 $\text{ft}^2/\text{sec.}$) Consequently, no modification to the exit velocities is required.

In step three, the induced velocity and turning angle are calculated. This calculation requires evaluation of the following equation seven times for each point analyzed:

$$
\begin{aligned}
q_n = -\frac{1}{4\pi}\sum_{j=0}^{\pm 3}\Biggl\{ & \Gamma_h\left[\frac{r_p - f d_h}{r_p^2 - 2 f d_h r_p + d_h^2} - \frac{r_p - f\left(\frac{r_h^2}{d_h}\right)}{r_p^2 - 2f\left(\frac{r_h^2}{d_h}\right) r_p + \left(\frac{r_h^2}{d_h}\right)^2}\right] + \\
& \Gamma_t\left[\frac{r_p - f d_t}{r_p^2 - 2 f d_t r_p + d_t^2} - \frac{r_p - f\left(\frac{r_t^2}{d_t}\right)}{r_p^2 - 2f\left(\frac{r_t^2}{d_t}\right) r_p + \left(\frac{r_t^2}{d_t}\right)^2}\right] - \\
& af\left[(r_t - \delta_t) - (r_h + \delta_h)\right] - \frac{1}{2}\left[f(2far_p + b) - ar_p\right] \ln \frac{(r_t - \delta_t)^2 - 2r_p f(r_t - \delta_t) + r_p^2}{(r_h + \delta_h)^2 - 2r_p f(r_h + \delta_h) + r_p^2} + \\
& (2far_p + b)\sqrt{1 - f^2}\left[\tan^{-1}\frac{\frac{1}{r_p}(r_t - \delta_t) - f}{\sqrt{1 - f^2}} - \tan^{-1}\frac{\frac{1}{r_p}(r_h + \delta_h) - f}{\sqrt{1 - f^2}}\right]\Biggr\} \; *
\end{aligned}
$$

---

* Reprinted from NACA RM E51G27

where:

J = integer
N = number of vanes in cascade
$f = \cos(2\pi J/N)$
Γ = circulation - ft^2/sec
r = radius - ft
d = radial distance from center-line to axis boundary layer vortex core - ft
δ = boundary layer thickness - ft
q = induced velocity - ft/sec
a, b = constants

Subscripts

n = normal to plane of trailing vorticity
h = hub
t = tip
p = point

This equation was programmed onto a computer and evaluated. The method used to estimate the boundary layer thickness was that presented by Reshotko et al[5]. The effects of the bellmouth and the inlet fairings were included, and the resulting boundary layer thickness was 0.160 inch on each wall.

In evaluating the equation, the last three terms were dropped since they reflect the effect of the main span vortex sheet and are not applicable to a free vortex design with constant circulation across the span. In addition, only seven vanes were considered for each calculation: a reference vane plus three vanes on each side. This approximation simplified the procedure and yielded sufficiently accurate results. Calculations were performed at 6 stations for both the root and the tip.

The change in the exit air angle ($\Delta\theta_i$) was calculated with the following equation:

$$\Delta\theta_i = K \tan^{-1}(q_n/V_{exit})$$

where
K = correlation factor

For these calculations, K was set at 0.45, which is the value suggested by Lieblein. Also good correlation has been obtained by Beatty et al[6] using a correlation factor of 0.45.

The actual turning angle is determined in step four, that is, the turning correction to the calculated inlet guide vane exit air angle. This calculation is straightforward and the inlet guide vane camber was modified to account for secondary flow effects as discussed in Section IV, Airfoil Design, A, Inlet Guide Vane.

APPENDIX D

Airfoil Design Data

AIRFOIL DESIGN DATA

Inlet Guide Vane

Inlet Root Diameter = 16.00 Inlet Tip Diameter = 31.00
Exit Root Diameter = 16.00 Exit Tip Diameter = 31.00
400 Series Airfoil, 27 Vanes

Percent Length	Root	10	20	30	40	50	60	70	80	90	Tip
Average Diameter	16.00	17.50	19.00	20.50	22.00	23.50	25.00	26.50	28.00	29.50	31.00
β_2*	4.70	4.90	5.10	5.30	5.50	5.70	5.90	6.10	6.30	6.50	6.70
β_3*	-45.33	-39.80	-36.24	-33.71	-31.64	-29.79	-28.21	-26.93	-25.99	-26.33	-28.43
ϕ	50.03	44.70	41.34	39.01	37.14	35.49	34.11	33.03	32.29	32.83	35.13
γ°	-24.80	-21.50	-19.37	-17.85	-16.55	-15.38	-14.35	-13.51	-12.90	-13.02	-14.17
t/c	0.09	0.09	0.09	0.09	0.09	0.09	0.09	0.09	0.09	0.09	0.09
σ	1.880	1.719	1.583	1.467	1.367	1.280	1.203	1.135	1.074	1.020	0.970
c	3.5	3.5	3.5	3.5	3.5	3.5	3.5	3.5	3.5	3.5	3.5
C_z	3.1772	3.2565	3.3019	3.3315	3.3550	3.3747	3.3908	3.4032	3.4117	3.4100	3.3935

Rotor

Inlet Root Diameter = 16.54 Inlet Tip Diameter = 31.00
Exit Root Diameter = 20.20 Exit Tip Diameter = 31.00
Circular Arc Airfoil, 28 Blades
Axial Tilt = 0 inch Tangential Tilt = 0.020 inch

Percent Length	Root	10	20	30	40	50	60	70	80	90	Tip
Average Diameter	18.37	19.633	20.896	22.159	23.422	24.685	25.948	27.211	28.474	29.737	31.0
β_1'*	33.90	37.20	39.80	42.15	44.25	46.25	48.15	50.05	51.95	53.95	56.00
β_2'*	-53.20	-36.80	-21.35	-8.60	1.20	9.55	17.10	23.50	29.40	35.25	40.95
ϕ	87.10	74.0	61.15	50.75	43.05	36.70	31.05	26.55	22.55	18.70	15.05
$\gamma^\circ_{rotating}$	-9.65	0.15	9.22	16.77	22.72	27.90	32.62	36.77	40.67	44.60	48.47
γ°_{static}	-9.65	0.36	9.76	17.62	23.84	29.25	34.16	38.47	42.49	46.49	50.39
t/c	0.08	0.076	0.072	0.068	0.064	0.06	0.056	0.052	0.048	0.044	0.04
σ	2.038	1.907	1.792	1.689	1.598	1.517	1.443	1.376	1.315	1.259	1.208
c	4.2	4.2	4.2	4.2	4.2	4.2	4.2	4.2	4.2	4.2	4.2
C_z	4.141	4.2	4.1457	4.0213	3.874	3.7118	3.5373	3.3641	3.1854	2.9905	2.7843
$\bar{X}$	2.1	2.1	2.1	2.1	2.1	2.1	2.1	2.1	2.1	2.1	2.1
$\bar{Y}$	0.6363	0.5397	0.4439	0.3696	0.3133	0.2675	0.2255	0.1911	0.1638	0.1344	0.1071

Note: Tilt is the offset of the center of gravity at the tip from a radial line and varies linearly from the average actual root center of gravity.

Stator - DCA

Double Circular Arc Airfoil - 63 Blades

Percent Length (Stator Inlet)	Root	10	20	30	40	50	60	70	80	90	Tip
Inlet Diameter	21.77	22.69	23.60	24.52	25.43	26.35	27.27	28.18	29.10	30.02	30.93
Outlet Diameter	22.78	23.53	24.32	25.11	25.92	26.14	27.54	28.38	29.21	30.05	30.92
β_2*	46.55	43.10	40.80	39.42	38.10	37.00	36.04	35.29	34.63	34.25	33.93
β_3*	-9.03	-8.50	-8.14	-7.94	-7.81	-7.73	-7.70	-7.71	-7.78	-7.91	-8.15
$\phi_{sp\ m}$	16.87	15.12	14.10	13.55	13.14	12.84	12.68	12.68	12.78	13.06	13.67
$\phi_{sb\ m}$	38.71	36.48	34.94	33.81	32.77	31.89	31.06	30.32	29.63	29.00	28.41
$\phi_{sp\ s}$	18.84	17.28	16.50	16.15	16.01	16.01	16.18	16.48	16.97	17.71	18.70
$\phi_{sb\ s}$	43.40	41.28	40.88	40.42	40.09	39.82	39.63	39.49	39.36	39.20	38.98
t/c	0.40	0.44	0.48	0.52	0.56	0.60	0.64	0.68	0.72	0.76	0.80
σ	1.940	1.870	1.803	1.740	1.682	1.627	1.576	1.525	1.480	1.437	1.397
c	2.155	2.155	2.155	2.155	2.155	2.155	2.155	2.155	2.155	2.155	2.155

Stator MCA-A

Multiple Circular Arc Airfoil - 63 Blades

Percent Length (Stator Inlet)	Root	10	20	30	40	50	60	70	80	90	Tip
Inlet Diameter	21.77	22.69	23.60	24.52	25.43	26.35	27.27	28.18	29.10	30.02	30.93
Outlet Diameter	22.78	23.53	24.32	25.11	25.92	26.74	27.54	28.38	29.21	30.05	30.92
β_2^*	44.57	40.69	37.94	36.12	34.56	33.25	32.15	31.27	30.65	30.36	31.58
β_3^*	-10.25	-9.44	-8.98	-8.72	-8.59	-8.51	-8.51	-8.60	-8.80	-9.20	-9.88
$\phi_{sp\ m}$	6.01	4.28	2.90	1.83	1.00	0.30	-0.25	-0.63	-0.80	-0.62	0.06
$\phi_{sb\ m}$	48.81	45.85	44.02	43.01	42.15	41.46	40.91	40.50	40.25	40.18	40.40
$\phi_{sp\ s}$	11.29	10.34	9.84	9.70	9.62	9.61	9.70	9.88	10.14	10.57	11.23
$\phi_{sb\ s}$	51.13	48.39	47.00	46.21	45.68	45.28	45.08	45.01	45.13	45.50	46.18
t/c	.40	.44	.48	.52	.56	.60	.64	.68	.72	.76	.80
σ	1.940	1.870	1.803	1.740	1.682	1.627	1.576	1.525	1.480	1.437	1.397
c	2.155	2.155	2.155	2.155	2.155	2.155	2.155	2.155	2.155	2.155	2.155
$a_{mc/c}$	.537	.537	.537	.538	.540	.543	.546	.549	.553	.557	.561
$a_{fwd/c}$	.324	.312	.306	.304	.304	.305	.309	.316	.325	.338	.357

Stator - MCA-B

Multiple Circular Arc Airfoil - 63 Blades

Percent Length (Stator Inlet)	Root	10	20	30	40	50	60	70	80	90	Tip
Inlet Diameter	21.77	22.69	23.60	24.52	25.43	26.35	27.27	28.18	29.10	30.02	30.93
Outlet Diameter	22.78	23.53	24.32	25.11	25.92	26.74	27.54	28.38	29.21	30.05	30.92
β_2^*	45.62	41.93	39.52	37.97	36.67	35.62	34.73	34.03	33.60	33.46	33.67
β_3^*	-11.40	-10.60	-10.16	-10.01	-9.97	-9.98	-10.11	-10.46	-10.93	-11.66	-12.81
$\phi_{sp\ m}$	7.95	6.63	5.70	5.14	4.72	4.41	4.21	4.19	4.32	4.64	5.84
$\phi_{m\ fwd}$	9.89	8.35	7.32	6.68	6.18	5.83	5.62	5.62	5.81	6.34	7.25
$\phi_{m\ aft}$	47.13	44.18	42.36	41.30	40.46	39.77	39.22	38.87	38.72	38.78	39.23
$\phi_{sp\ s}$	11.28	10.33	9.86	9.68	9.60	9.60	9.70	9.90	10.18	10.60	11.23
$\phi_{s\ fwd}$	14.11	13.20	12.75	12.68	12.69	12.78	13.00	13.36	13.81	14.40	15.32
$\phi_{s\ aft}$	49.73	47.15	45.69	45.01	44.55	44.36	44.17	44.28	44.63	45.30	46.48
t/c	.40	.44	.48	.52	.56	.60	.64	.68	.72	.76	.80
σ	1.940	1.870	1.803	1.740	1.682	1.627	1.576	1.525	1.480	1.437	1.397
c	2.155	2.155	2.155	2.155	2.155	2.155	2.155	2.155	2.155	2.155	2.155
$a_{mc/c}$	.554	.554	.555	.556	.559	.562	.566	.571	.577	.585	.596
$a_{fwd/c}$	.401	.398	.397	.398	.401	.407	.416	.427	.442	.462	.491
$a_{sp/c}$	.321	311	.305	.303	.304	.306	.310	.317	.327	.341	.361
Z	12.0	12.0	12.0	12.0	12.0	12.0	12.0	12.0	12.0	12.0	12.0

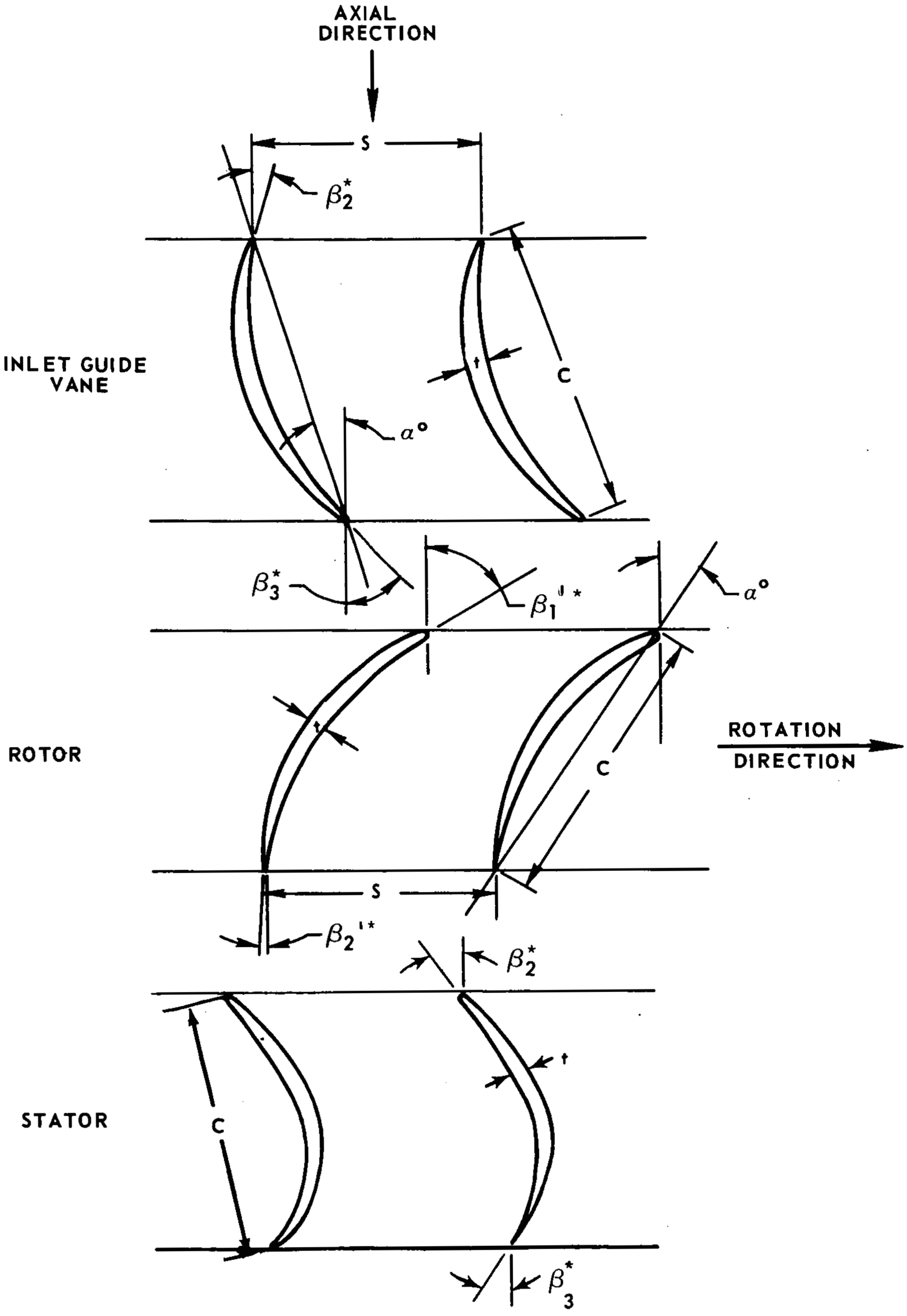

Figure D-1 Airfoil Geometry Symbols

APPENDIX E

References

REFERENCES

1. Cullom, R. C., Montgomery, J. C., and Yasaki, P. T. Experimental Performance of a 0.35 Hub-Tip Radius Ratio Transonic Axial-Flow-Compressor Stage Designed for 40 Pounds Per Second Per Unit Frontal Area. NACA RM E 58D04a, September, 1958.

2. Lieblein, S., and Ackley, R. H. Secondary Flows in Annular Cascades and Effects of Flow in Inlet Guide Vanes. NACA RM E51G27, August, 1951.

3. Johnsen, I. A., and Bullock, R. O. (eds.) Aerodynamic Design of Axial Flow Compressors. NASA SP-36, 1965.

4. Tysl, E. R., Schwenk, F. C., and Watkins, T. B. Experimental Investigation of a Transonic Compressor Rotor with a 1.5-Inch Chord Length and an Aspect Ratio of 3.0. NACA RM E54L31, March, 1955.

5. Reshotko, E., and Tucker, M. Approximate Calculation of the Compressible Turbulent Boundary Layer with Heat Transfer and Arbitrary Pressure Gradient. NACA TN 4154, December, 1957.

6. Beatty, L. A., Savage, M., and Emery, J. C. Experimental Investigation of Flow Through Three Highly Loaded Inlet Guide Vanes Having Different Spanwise Circulation Gradients. NACA RM L52D25a, July, 1952.

7. Schwenk, F. C., Lewis, G. W., and Hartmann, M. J. A Preliminary Analysis of the Magnitude of Shock Losses in Transonic Compressors. NACA RM E57A30, March, 1957.

8. Lieblein, S., Schwenk, F. C., and Broderick, R. L. Diffusion Factor for Estimating Losses and Limiting Blade Loadings in Axial-Flow-Compressor Blade Elements. NACA RM E53D01, June, 1953.

9. Shepherd, D. G. Principles of Turbomachinery. New York: The Macmillan Company, 1965.

10. Young, W. W. The Experimental Investigation of a Research Transonic Inlet Stage Compressor. WADC TR 57-207, 1957.

11. Klapproth, J. F., Jacklitch, J. J. Jr., and Tysl, E. R. Design and Performance of a 1400-Foot-Per-Second-Tip-Speed Supersonic Compressor Rotor. NACA RM E55A27, April, 1955.